A New Data Driven Bayesian Inversion of Fluvial Topography Clarifies the Tectonic History of the Corinth Rift and Reveals a Channel Steepness Threshold

S. F. Gallen, D. Fernández-Blanco

JGR Earth Surface

RESEARCH ARTICLE
10.1029/2020JF005651

A New Data-Driven Bayesian Inversion of Fluvial Topography Clarifies the Tectonic History of the Corinth Rift and Reveals a Channel Steepness Threshold

S. F. Gallen[1] and D. Fernández-Blanco[2,3]

[1]Department of Geoscience, Colorado State University, Fort Collins, CO, USA, [2]Institut de physique du globe de Paris, CNRS, Université de Paris, Paris, France, [3]Now at Consejo Superior de Investigaciones Científicas (CSIC), Instituto de Ciencias del Mar (ICM), Passeig Marítim de la Barceloneta, Barcelona, Spain

Key Points:

- We present a new Bayesian approach to simultaneously invert river profiles and marine terraces for tectonic and geomorphic model parameters
- This approach is applied to the Corinth Rift and offers new insights into the rift's recent (< 1 Myr) tectonic and geomorphic history
- The tectonic parameters are consistent with existing studies, and the geomorphic parameters suggest a threshold channel steepness index

Supporting Information:

- Supporting Information S1

Correspondence to:
S. F. Gallen,
sean.gallen@colostate.edu

Citation:
Gallen, S. F., & Fernández-Blanco, D. (2021). A new data-driven Bayesian inversion of fluvial topography clarifies the tectonic history of the corinth rift and reveals a channel steepness threshold. *Journal of Geophysical Research: Earth Surface*, *126*, e2020JF005651. https://doi.org/10.1029/2020JF005651

Received 10 APR 2020
Accepted 7 JAN 2021

Abstract Landscape evolution models that invert topography for rock uplift can improve our understanding of both tectonic and geomorphic processes when properly constrained with data. Here we present a flexible, data-driven Bayesian approach to invert fluvial topography for tectonic and geomorphic model parameters and apply it to a case study, the uplifting footwall of the Corinth Rift, Greece. We invert transient river profiles and up-flexed marine terraces to resolve seven unknown parameters in a regional-to-flexural uplift tectonic model and the stream power incision model. The best-fit tectonic parameters are consistent with independent data and predict block uplift rates of ~0.1 mm yr^{-1} that changed to flexural uplift rates of ~1.6 mm yr^{-1} at ~0.6 Ma, as the master normal fault initiated. Similarly, the best-fit geomorphic parameters predict sediment flux consistent with the offshore record and erodibility consistent with previous studies. However, the drainage area exponent, m, of ~2, and slope exponent, n, of ~7, are unusually high, indicating a threshold channel steepness where fluvial topography is largely insensitive to rock uplift rate >0.05 mm yr^{-1}. Analysis indicates channels narrow to accommodate enhanced uplift rates, but channel narrowing only partially explains our results, suggesting that other processes not accounted for in the generic stream power model are also relevant to bedrock river incision in Corinth. Our results help clarify the tectonic and geomorphic evolution of the Corinth Rift, have important implications for studies that invert topography for rock uplift histories, and provide insight into potential limitations of some long-term river incision models.

Plain Language Summary Landscapes are influenced by many factors, including climate, land motion, and the strength of rocks. To understand and reproduce the evolution of landscapes, scientists use numerical models to approximate the physics that shape topography. Armed with these mathematical techniques, it is, in principle, possible to "unwind" the current landscape to understand the history of past events and processes that shaped it. In this work, we present models that use data from rivers and uplifted fossil beaches to understand the history of vertical land movement and the physical processes that gave rise to a well-known site in the north of the Peloponnese, Greece. Our results provide specific insight into the study area and, more generally, have important implications for the processes that erode and transport sediment from continental settings. Our models are flexible and can include other types of data that may be important in other sites. Our findings highlight several key questions that merit further research to understand the processes that control the long-term evolution of continental landscapes.

1. Introduction

A fundamental goal of tectonic geomorphology is the quantitative extraction of tectonic and geomorphic signals from topography. Earth surface process models predict landscape response to tectonic forcing whereby topography, erosion rates, and sediment production transiently adjust to changes in tectonic boundary conditions (Beaumont et al., 1992; Howard et al., 1994; Koons, 1989; Tucker & Slingerland, 1996; Whipple & Tucker, 1999). Empirical studies of many tectonically active landscapes have backed up model predictions and show that topography steepens, and erosion rates increase in areas experiencing more rapid rock uplift (Cyr et al., 2010; DiBiase et al., 2010; Harkins et al., 2007; Kirby & Whipple, 2001, 2012; Ouimet et al., 2009; Miller et al., 2013; Safran et al., 2005; Snyder et al., 2000). Furthermore, studies have shown

that changes in the base level fall rate (e.g., a shift in rock uplift rate) generate knickpoints that migrate upstream, translating the base level signal throughout the landscape (Berlin & Anderson, 2007; Crosby & Whipple, 2006; Gallen, 2018; Gallen et al., 2013; Miller et al., 2013). These modeling and empirical studies show that landscapes, and especially river networks, are sensitive recorders of tectonic activity (e.g., Kirby & Whipple 2012).

Inspired by this research, a growing body of literature uses landscape evolution equations to invert topography for rock uplift histories (e.g., Fox et al. 2014; Glotzbach, 2015; Goren et al., 2014; Pritchard et al., 2009; Roberts & White, 2010; Rudge et al., 2015). These studies mostly rely on the detachment-limited stream power incision model to predict the long-term evolution of river networks. This model approximates bedrock incision rate as the product of a power law of upstream drainage area (a proxy for discharge) and a power law of local channel slope scaled by a constant of erodibility (Howard, 1994; Howard & Kerby, 1983; Whipple & Tucker, 1999). Many of these studies assume that the power-law exponent on slope, n, is 1 to linearize the inverse problem, allowing for the application of efficient linear inverse theory (Fernandes et al., 2019; Fox et al. 2014; Goren et al., 2014; Rudge et al., 2015). Nonlinear inversions have also been applied in several cases (Croissant & Braun, 2014; Glotzbach, 2015; Pritchard et al., 2009; Roberts & White, 2010).

Other studies use similar techniques together with geological constraints to calibrate and vet earth surface process models (Barnhart et al., 2020a, 2020b, 2020c). These studies have used the stream power model, as well as other more sophisticated expressions for landscape evolution, in an effort to broaden our understanding of the specific equations and dominant earth surface processes needed to explain particular aspects of observed topography (Barnhart et al., 2020a, 2020b, 2020c). These studies are thus usually less concerned with resolving the uplift pattern or the underlying tectonic or geodynamic processes.

Several studies jointly invert topography for tectonic and geomorphic variables using nonlinear inversions (e.g., Croissant & Braun, 2014; Glotzbach 2015). Croissant and Braun (2014) test the ability of a nonlinear inversion of topography to constrain parameters in the stream power model from synthetically derived landscapes generated with known parameters. They also apply this approach using a digital elevation model (DEM) from the Southern Alps of New Zealand to constrain the stream power parameters and a simple tectonic model of rock uplift. Croissant and Braun (2014) demonstrate that significant parameter trade-offs exist that make it difficult to constrain the stream power model when inverting topography alone. Glotzbach (2015) uses a similar inversion technique but incorporates geological observables, including low-temperature mineral cooling histories and measurements of cosmogenic nuclides in river sands, formally into the inversion. Glotzbach (2015) shows that rock uplift history and stream power parameters can both be resolved with this data-driven approach, yet, when the analytical data is removed from the inversion, the history of uplift cannot be accurately recovered. These studies thus show that nonlinear inversions of topography coupled with geological data can provide meaningful insight into both tectonic and earth surface processes.

Here we present a new Bayesian approach to invert fluvial topography and field data for tectonic and geomorphic model parameters simultaneously. The method utilizes the stream power incision model and longitudinal river profiles and can flexibly incorporate different types of geological data to constrain the inversion, such as erosion rates, marine and river terraces, and sediment flux records. We apply this approach to shed light on the tectonic and geomorphic processes governing the evolution of the uplifting southern margin of the Corinth Rift in central Greece (Figure 1).

Our case study focuses on the eastern portion of the southern margin of the Corinth Rift, Greece (Figure 1). This intracontinental rift is ideal for our investigation, for it is very well studied, and the wealth of existing data can both inform our inversion and allow detailed comparisons between model predictions and geological constraints not used in the inversion. The general aspects of the tectonic evolution of the rift are understood. A protracted period of distributed extension and concomitant, slow regional uplift was followed by rapid establishment of the current rift bounding fault and flexural uplift of the southern rift margin at ~2–0.6 Ma (Armijo et al., 1996; Brasier et al., 2011; de Gelder et al., 2019; Ford et al., 2007, 2017; Nixon et al., 2016; Rohais et al., 2007). The recent spatial and temporal pattern of flexural uplift is recorded, at least since ~0.4 Myr, by a spectacular, well-preserved suite of marine terraces along the eastern edge of the rift (Figures 1 and 2; Armijo et al., 1996; de Gelder et al., 2019). Whereas the cumulative effect of lithospheric

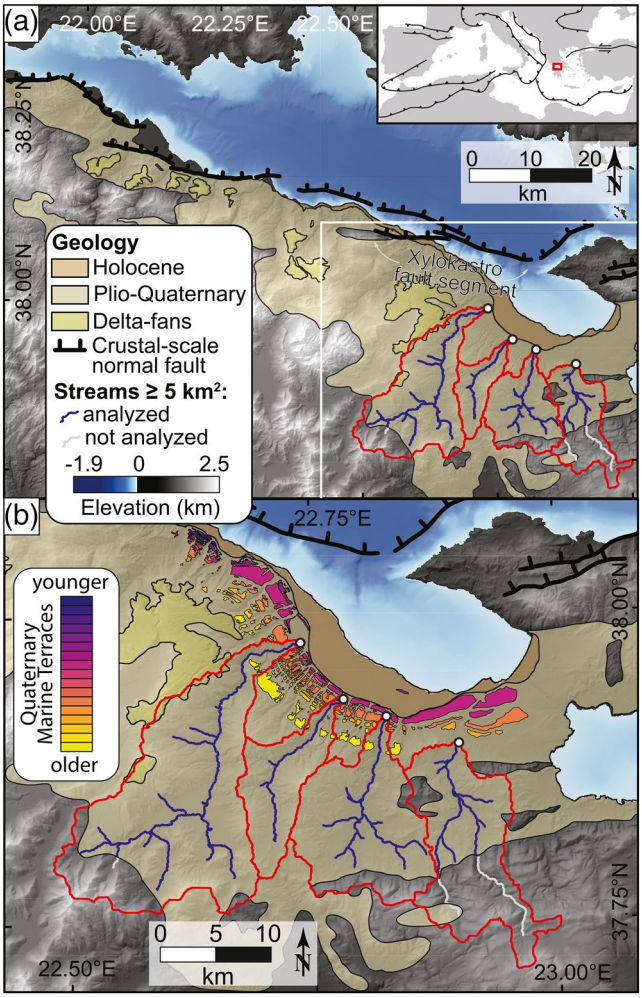

Figure 1. Location, tectonic setting, and simplified geology of the study area. (a) Map of the topography and bathymetry of the Corinth Rift. The white frame shows the area of interest for this study with the four drainage basins outlined in red. The drainage basins were delineated upstream of obviously alluviated lower reaches based on inspection of satellite imagery. The upper right inset shows a simplified tectonic map of the Mediterranean with some of the major plate boundaries noted. The small red box shows the location of the map in (a). (b) Shaded relief map with simplified geology of the eastern portion of the Corinth footwall, which we refer to as the Eastern Sector, as highlighted by the white frame in (a). The Eastern Sector drainage basins and rivers studied are also shown. Marine terraces shown as mapped by de Gelder et al. (2019).

flexure along the entire rift margin is recorded in its topography, its rivers record the associated change in the rate of uplift as a series of large, upstream-migrating fluvial knickpoints (Figure 2e; Fernández-Blanco et al., 2019, 2020). In this study, we take advantage of the transient river profiles, in conjunction with the suite of marine terraces, to refine the tectonic evolution of the eastern portion of the southern margin of the Corinth Rift, and learn more about how river systems respond to tectonic perturbations.

Our study has two primary goals. Our first goal is to better resolve the initiation time of the modern rift bounding fault by extending the history of rock uplift further back in time than is possible with the marine terrace record. Our second goal is to constrain the stream power parameters that are needed to predict the topographic evolution, erosion rates, and sediment flux of the southern rift margin through time. Through this investigation, we demonstrate that valuable information on both tectonic and geomorphic processes can be retrieved from nonlinear data-driven inversions of fluvial topography.

2. Background

2.1. Tectonic and Geologic Setting

The Corinth Rift is the fastest-extending intracontinental rift among those that accommodate lithospheric stretching in the Aegean. Extension in the Aegean occurs due to the retreat of the subducting African slab and, more recently, due to changes in the regional stress field imposed by the southwestward propagation of the North Anatolian Fault into the northern Aegean (Armijo et al., 1996; Jolivet & Brun, 2010; Jolivet et al., 2013; Le Pichon et al., 1981). The present-day Corinth Rift is an asymmetric half-graben with a steep, high-relief southern flank and a gentle, lower-relief northern flank (Figure 1). The rift is controlled by a ~130 km long, ~60° northward dipping composite normal fault system composed of 10–25 km long en echelon segments (Figure 1; e.g., Armijo et al., 1996; Fernández-Blanco et al., 2019; Gawthorpe et al., 2017). This contemporary master fault system reaches, *ad minimum*, the base of the seismogenic layer (Armijo et al., 1996; Bell et al., 2017; Fernández-Blanco et al., 2019), and is here termed the Corinth Fault System (CFS). The CFS initiated in the recent geologic past (~2–0.6 Ma) based on evidence that is discussed below.

The Corinth Rift strikes obliquely to the structural grain of the Hellenide nappes that stacked and thickened the crust during Eocene-to-Late Miocene accretion associated with the Hellenic Subduction Zone (e.g., Bonneau, 1984; Jolivet & Brun, 2010). The Hellenide units in Corinth consist of deformed phyllites, ophiolites, flysch, and carbonates that now form "basement" rock surrounding the modern rift (Armijo et al., 1996). Basement rocks are cut by the steep CFS, that uplifts in its footwall lightly deformed, weakly lithified, and poorly indurated basin-fill sediments, consisting of interbedded lacustrine, fluvial sands and silts, fan-delta conglomerates, and marine marls of Plio-Pleistocene age (e.g., Armijo et al., 1996; Ori, 1989). This stratigraphy primarily reflects glacio-eustatic variations in a confined setting that resulted in lacustrine environments during sea-level lowstands and deposition of marine sediments during sea-level highstands (e.g., Collier, 1990; de Gelder et al., 2019).

2.2. Fault Initiation and Earlier Uplift History

The establishment of the CFS caused rapid flexural uplift of the footwall and demarcates a geologically-recent (<2 Ma) transition from a pre-CFS regional uplift history (e.g., Armijo et al., 1996; de Gelder

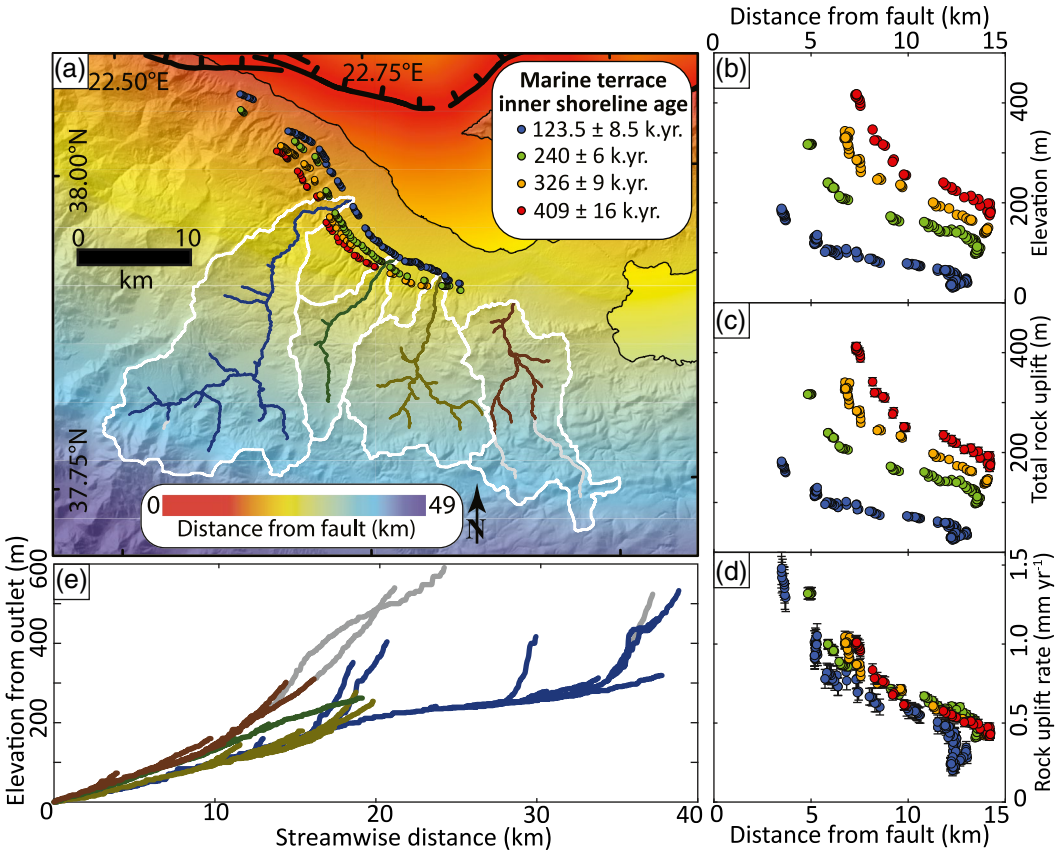

Figure 2. Geologic and geomorphic evidence of recent deformation associated with slip on the Corinth Rift master fault (CFS) in the Eastern Sector. (a) Map of Euclidean distance from the CFS fault trace (in black) as a warm-to-cool color scheme, and the studied drainage basins as white polygons. River networks of the four studied drainage basins are shown as lines colored according to each drainage basin; the gray portions of the river networks were excluded from our analysis because they flow over different rock units than the majority of the basin. Paleoshoreline angles of the four most prominent and extensive marine terrace levels (mapped by de Gelder et al., 2019) are shown as circles, and colored according to their estimated ages: 123.5 ± 8.5 ka (blue); 240 ± 6 ka (green); 326 ± 9 ka (orange); and 409 ± 16 ka (red). (b, c, d) Show the elevation, total rock uplift, and rock uplift rate, respectively, for the four marine terrace inner paleoshoreline angles shown in (a), plotted as a function of Euclidean distance from the fault. Note the up-flexed deformation of the marine terraces. (e) Shows longitudinal river profiles of the stream network used in the data analysis colored according to the drainage basin networks shown in a (gray portions excluded from our analysis as noted above). Note the large knickpoint in the river profile at ~20 km upstream.

et al., 2019; Fernández-Blanco et al., 2019, 2020). Relevant to our study is the uplift history of the eastern portion of the southern rift margin that is currently bound by the Xylokastro Fault segment, which we simply refer to as the "Eastern Sector" (Figure 1). A broad time range for the onset of the Eastern Sector fault segment from ~2,000 to 800 kyr is inferred from onshore stratigraphy related to a series of uplifted fan deltas (Gawthorpe et al., 2017). Linear extrapolation of the Late Pleistocene marine terraces (Armijo et al., 1996; de Gelder et al., 2019) and dated calcite cement in terrace deposits (Causse et al., 2004) imply fault initiation at ≤1,000 kyr. The up-flexed marine terraces in the CFS footwall provide an age of ~700–600 kyr for the initiation of the Xylokastro Fault (Armijo et al., 1996; de Gelder et al., 2019). A similar onset time of 800–600 kyr is estimated from the coalescence of offshore depocenters in the CFS hanging wall (Nixon et al., 2016). Depositional ages and U-Th dating of tufa in uplifted fan deltas suggests fault onset between ~700 and 600 kyr (Brasier et al., 2011; Ford et al., 2007, 2017; Rohais et al., 2007). Based on the age of uplifted deltas, the up-flexed marine terraces, and the deepest offshore sediments, de Gelder et al. (2019) infer that ~60%–70% of the deformation associated with the CFS structure occurred in the last ~610 ka.

Estimates of the uplift rates and patterns relating to the period of distributed extension preceding the establishment of the CFS are more difficult to constrain due to a lack of necessary observables. Using a mechan-

ical model of lithospheric deformation calibrated with the Eastern Sector marine terraces, Armijo et al. (1996) suggested a modest regional uplift rate of ~0.2 mm yr^{-1} before initiation of the CFS. Turner et al. (2010) estimated similar contemporary rates of isostatically driven regional uplift that might apply to pre-CFS uplift rates. However, structural and sedimentological evidence shows that normal faults in the southern rift margin progressively migrated northward to their current position (e.g., Armijo et al. 1996; Ford et al., 2017; Sorel, 2000). These observations imply a variable pattern of uplift in the footwall of the present-day CFS before its establishment. Nonetheless, based on the previous lines of evidence and terrestrial facies in small basin deposits, the uplift rates during preceding modern fault initiation were likely between 0 and 0.3 mm yr^{-1} (e.g., Turner et al., 2010).

2.3. Marine Terraces and Pleistocene Rock Uplift History

The eastern portion of the southern rift margin preserves a spectacular suite of up-flexed Pleistocene marine terraces (Figures 1a, 2a, 2b, 2c, and 2d). These terraces cut broad abrasion platforms and paleo-sea cliffs into the Plio-Pleistocene basin fill and are typically associated with 2–6 m of erosionally resistant, well-cemented beach and coastal deposits (Armijo et al., 1996; de Gelder et al., 2019). Recently, de Gelder et al. (2019) identified 16 unique terraces using high-resolution digital surface models to update and revise the original mapping by Armijo et al. (1996) (Figure 1b). Several geochronological constraints based on U-Th dating of corals preserved in terrace deposits yield ages consistent with the timing of glacio-eustatic highstands (Collier et al., 1992; Dia et al., 1997; Leeder et al., 2003). These findings align with physical models for marine terrace construction whereby terraces form during periods of relative sea-level stability (e.g., equal rates of rock uplift and sea level rise) and are abandoned during relative sea-level fall (Anderson et al., 1999). Accordingly, age determination of undated terraces can be achieved through correlation of the elevation of marine terrace inner shoreline angles (ISA) (the position considered the best estimate of paleo-sea level) to the timing of known glacio-eustatic highstands (e.g., Gallen et al., 2014; Lajoie, 1986; Merritts & Bull, 1989; Ott et al., 2019).

Using the existing geochronological data and this approach, de Gelder et al. (2019) confidently estimate the ages of the four most extensive and well-preserved terraces as 123.5 ± 8.5 ka, 240 ± 6 ka, 326 ± 9 ka, and 409 ± 16 ka Figures (2a, 2b, 2c, and 2d, Table S1). Using these correlations, de Gelder et al. (2019) show that the rates of rock uplift in the Eastern Sector of Corinth Rift exponentially decay from ~1.3 mm yr^{-1} for sites closest to the CFS to ~0.3 mm yr^{-1} over a distance of ~25 km, consistent with the earlier work by Armijo et al. (1996). The exponential deformation pattern recorded by these terraces is consistent with models of lithospheric flexure of a broken plate Figures (2a, 2b, 2c, and 2d; Armijo et al., 1996; de Gelder et al., 2019; Nadai, 1963). Extrapolation of this flexural uplift pattern to the fault trace suggests maximum footwall uplift rates of 1.6–1.7 mm yr^{-1} (de Gelder et al., 2019).

2.4. Climate

Watkins et al. (2018) recently compiled a series of data sets to synthesize the climate history in Corinth over the last ~130 ka that we summarize here. Records from contemporary (ca. 1950–2000) weather stations indicate mean annual temperature and mean annual precipitation of ~14.5°C and ~400–800 mm yr^{-1}, respectively (Figure S1; Hijmans et al., 2005). Paleoclimate in the region is largely deduced from pollen records and global circulation models (GCMs). The pollen record shows some increasing aridity during the last glacial maximum (LGM) and alternating cool/drier and warmer/wetter periods further back in time (Tzedakis, 1999; Tzedakis et al., 2002). The GCMs indicate that mean annual temperature and mean annual precipitation during the LGM ranged between ~8.8 and 9.6°C, and between 716 and 977 mm yr^{-1}, respectively. Considering the imprint of global climate change on the geomorphic record in Corinth (e.g., marine terraces associated with glacio-eustacy), the pollen records and GCMs suggest that regional climate over the last ~130 ka remained relatively stable. Given the lack of records of terrestrial climate prior to this period, we make the simplifying assumption that climate has been roughly stable over the Quaternary.

2.5. Fluvial Geomorphology

As for many tectonically active mountain river systems, most channel reaches in Corinth can be characterized as bedrock rivers, i.e. rivers with bedrock channel walls and patches of alluvium and bedrock in the active channel that reflect elevated sediment transport capacity relative to sediment supply (Whipple, 2004; Zondervan et al., 2020). Nearly all of the major river systems in Corinth exhibit large knickpoints or knickzones in their longitudinal profiles interpreted to reflect the ongoing adjustment of the river channels to the change in uplift rate associated with the establishment of the CFS (Figure 2e; Demoulin et al., 2015; Fernández-Blanco et al., 2019, 2020). Within the knickzones, river valleys are generally narrow relative to downstream reaches and form gorges in some locations (Karymbalis et al., 2016; Zondervan et al., 2020). Upstream and downstream of knickzones, river valleys widen slightly and are more alluviated relative to reaches within the knickzone (e.g., Seger & Alexander, 1994; Zondervan et al., 2020).

2.6. The Stream Power Model, Fluvial Topography, and Empirical Calibration

The detachment-limited stream power model (Howard & Kerby, 1983; Howard, 1994; Whipple & Tucker, 1999) is most appropriate for bedrock rivers and is, therefore, applicable to river systems in Corinth. This model is justified by empirically derived scaling approximations between upstream drainage area and variables relevant to the magnitude of shear stress along the channel bed imparted by streamflow, such as discharge and channel geometry (e.g., width). The goal of the stream power model is to capture the idea that bedrock erosion rate is a power law of excess shear stress on the channel bed cast as (Howard, 1994; Tucker & Bras, 2000);

$$\varepsilon = k_e\left(\tau_s - \tau_c\right)^a, \quad \tau_s > \tau_c \tag{1}$$

or as (DiBiase & Whipple, 2011; Lague et al., 2005):

$$\varepsilon = k_e\left({\tau_s}^a - {\tau_c}^a\right), \tau_s > \tau_c \tag{2}$$

where ε is the vertical incision rate into bedrock, τ_s and τ_c are the basal and critical shear stresses, respectively, k_e is a constant describing the efficiency of erosion, and a is an exponent related to the dominant incision process (Whipple et al., 2000). Using the empirical scaling approximation mentioned above, it is possible to arrive at a simplified empirical model for the long-term rate of river incision into bedrock, E, designed to capture the essence of the above equations:

$$E = KA^mS^n \tag{3}$$

where K is a constant that describes erodibility, A is the drainage area (a proxy for discharge), S is the local channel slope, and m and n are positive constants.

The erodibility constant incorporates a number of factors such as bedrock properties, mean runoff, and other hydrologic variables. The m and n exponents describe characteristics of hydrology, hydraulic scaling, and incision process. The ratio of these exponents apparently covaries, as most empirical studies of equilibrium river profiles find values between ~0.3 and 0.7, and theoretical considerations suggest that their ratio falls between ~0.4 and 0.6 (e.g., Kirby & Whipple, 2012). Equation (3) is perhaps the most widely used model for long-term river incision, and we use it in our inversion of fluvial topography; however, we recognize its limitations and return to the assumptions made by this model, such as width-drainage area scaling and the potential influence of sediment and incision thresholds on empirically calibrated parameters (cf. Lague, 2014), in the discussion.

Fluvial topography can be linked to rock uplift, U, through the stream power incision model, by solving Equation 3 for local channel slope and comparing it to the empirical scaling between local channel slope and upstream drainage area for graded, equilibrated river channels (e.g., Kirby & Whipple, 2001, 2012; Snyder et al., 2000; Wobus et al., 2006). Equilibrated river profiles exhibit a power-law scaling between local channel slope and upstream drainage area, commonly referred to as Flint's law, defined as (Flint, 1974; Hack, 1957; Morisawa, 1962):

$$S = k_s A^{-\theta} \tag{4}$$

where k_s is the steepness index, and θ is the channel concavity index. Solving Equation 3 for local channel slope yields a similar power-law relationship between local channel slope and upstream area, suggesting that (Kirby & Whipple, 2001, 2012; Snyder et al., 2000; Wobus et al., 2006):

$$k_s = \left(\frac{E}{K}\right)^{\frac{1}{n}} \tag{5}$$

and,

$$\theta = m / n \tag{6}$$

At steady-state, $E = U$ in Equation 5, which highlights how the channel steepness index relates topographic form to erosion rate and rock uplift rate. The m to n ratio, θ (a.k.a. the channel concavity index), is thought to be insensitive to tectonic perturbations. Given this, θ is often fixed to a value of ~0.5 to derive a normalized steepness index k_{sn} that is also equal to the term on the right-hand side of the equation in Equation 5 (Kirby & Whipple, 2012; Wobus et al., 2006).

Equations 3 through 6 also provide a way to empirically calibrate the stream power model, by combining analysis for fluvial topography with incision rate or erosion rate data. The m to n ratio can be estimated empirically in several ways, such as a power-law regression through slope-drainage area data (e.g., Wobus et al., 2006) or via analysis of χ-transformed river profiles (Perron & Royden, 2013). The stream channel metric, χ, is the path integral of the inverse of upstream drainage area raised to an exponent equal to the m to n ratio. The χ transformation effectively linearizes river profiles in plots of χ versus elevation, known as χ-plots, making k_{sn} the slope of a χ-plot.

After the m to n ratio is determined, the normalized steepness index is calculated for a river reach or an entire drainage basin via a normalized power-law regression of slope-drainage area data or linear regression of a χ-plot. To determine K, m, and n, a series of incision or erosion rates are measured, usually from dated river terraces or basin average erosion rates derived from cosmogenic nuclides, for river reaches or drainage basins, respectively, that are assumed to be in quasi-equilibrium. A power-law regression through the E and k_{sn} data is then used to determine K and n (Equation 5), and m is derived from the assumed m to n ratio (Equation 6).

2.6.1. Estimates of the Erodibility Parameter, *K*

Calibration of the stream power model from river systems globally suggests the erodibility parameter, K, varies over four to five orders of magnitude (Harel et al., 2016; Hilley et al., 2019; Stock & Montgomery, 1999). It is important to note that the particular value of K is dependent on values of m and n, such that K values determined for different m and n values are not directly comparable. A simple way to conceptualize this point is based on Equation 5. If we assume the same river profile concavity (i.e., fixed m to n ratio) for a steady-state river, then $K = U k_s^{-n}$. From this, if we assume an uplift rate of 1 mm yr^{-1}, a steepness index of 100 m, and a constant m to n ratio with assumed n values of 0.5, 1, and 2, K is 1×10^{-4} m$^{1-2\,\mathrm{m}}$ yr^{-1}, 1×10^{-5} m$^{1-2\,\mathrm{m}}$ yr^{-1}, 1×10^{-7} m$^{1-2\,\mathrm{m}}$ yr^{-1} for each n value, respectively. This has two implications relevant to this study. First, K values must be "normalized" to reference m and n values for comparison, and, second, the range of K used in our inverse model priors (discussed below) can be much greater than the typically observe range for the dependence of K on a given m and n value.

Several studies calibrate versions of the stream power erodibility parameter for river systems in Corinth, assuming that $m = 0.5$ and $n = 1$. Pechlivanidou et al. (2019) use volumes of offshore sediment deposited in the Gulf of Corinth to calibrate a landscape evolution model that predicts sediment flux from the rift margins. They place bedrock lithology into three broad categories based on slope and elevation, and iteratively solve for the erodibilities that, based on the stream power model, best produce the observed sediment volumes. Their analysis finds that K varies from ~1.5×10^{-6} to 4×10^{-6} m$^{1-2\,\mathrm{m}}$ yr^{-1}, the higher values being rep-

resentative of lithological units comparable to those in the catchments studied here. Zondervan et al. (2020) conducted a detailed field investigation of the Vouraikos River, a river basin westward of the Eastern Sector. These authors use hydraulic geometry, calculations of bank-full discharge, and estimates of the contemporary rock uplift velocity to determine erodibility for several rock units incised by the river. The incision model calibrated by Zondervan et al. (2020) is a variant of the stream power model that explicitly accounts for channel geometry and discharge, which in our equations are represented by a scaling relationship between both variables and drainage area. Converting their erodibility to stream power units assuming that $m = 0.5$ and $n = 1$ yields a value of K of $\sim 6 \times 10^{-6}$ $m^{1-2\,m}$ yr^{-1} for rock types comparable to those in the Eastern Sector.

2.6.2. Estimates of the Drainage Area Exponent, *m*, and the Slope Exponent, *n*

There are only a few empirical estimates of m and n in the literature, and, to our knowledge, m and n have not been empirically calibrated in Corinth. Lague (2014) used the empirical approach described in Section 2.6 to determine m and n values for ten globally distributed data sets thought to be at least locally in steady-state and found that m ranges from ~0.5 to 2 and n from ~1 to 4. Harel et al. (2016) conducted a global analysis of cosmogenic beryllium-10 (^{10}Be)-derived basin average erosion rates and DEMs to calibrate stream power parameters empirically. Using a fixed concavity of 0.5, they report a mean ($\pm 1\sigma$) m of ~1.35 ($\pm$ 1.45) and a range of ~−4.5 to 4.5, and a mean ($\pm 1\sigma$) n of ~2.7 ($\pm$ 2.9) and a range of ~−9 to 9. The large spread in values from this analysis is likely due to the fact that they include transient landscapes and measurements from basins that span geologic, tectonic, and environmental diversity (e.g., variations in rock type, uplift rate, climate, and rainfall) that can affect empirical calibrations of this kind. Owing to these complexities, global means and associated 1σ uncertainties reflect a more conservative and reasonable range of n and m values.

Hilley et al. (2019) also applied this empirical approach to calibrate the stream power model using ^{10}Be-derived basin average erosion rates and k_{sn} measurements from drainage basins floored by granitic bedrock in tropical climates. The 14 basins included in their analysis span a range of erosion rates from $\sim 5 \times 10^{-3}$ mm yr^{-1} to ~7 mm yr^{-1}, and they show that k_{sn} is relatively constant for erosion rates ≥~0.03 mm yr^{-1}. Hilley et al. (2019) then use a global compilation of ^{10}Be-derived erosion rates and an analysis of digital topography to support this finding showing that there is a threshold steepness index where fluvial topography is no longer sensitive to changes in erosion rate. They use this evidence to suggest that there are limitations in our current understanding of channel incision processes. We note that the general insensitivity of k_{sn} to changes in erosion rate above this threshold is indicative of extremely high n values and might result from processes that are not explicitly accounted for in the generic stream power model.

3. Materials and Methods

In this study, we combine a simplified tectonic model for the geologically-recent evolution of the Corinth Rift with the stream power incision model, incorporating data from deformed marine terraces and river profiles in a Bayesian framework that inverts for free parameters in each model. We model the rock uplift history and evolution of the four drainage basins in the Eastern Sector (Figures 1 and 2). We select this location for its impressive marine terrace record and because the river basins are largely contained within a single geologic unit (Figure 1). Below, we first describe the data sets and forward models used for our analysis. We then highlight the key modeling assumptions required to set up the inverse problem in a simplified, tractable framework. Finally, we detail our inverse modeling approach.

3.1. Data sets

We use TopoToolbox 2 and ChiProfiler to model surface hydrology and define channel networks and profiles on a 20 m horizontal-resolution SPOT5 DEM (Figures 1 and 2e; Gallen & Wegmann, 2017; Schwanghart & Scherler, 2014). The channel network was delineated as areas draining 5 km^2, and no smoothing was conducted to augment the channel geometry. We restricted our analysis to locations upstream of areas with visual evidence of thick alluvial fill along a Holocene coastal platform to ensure that the studied rivers are characterized by bedrock channels (Figure 1).

Our study uses marine terrace inner shoreline angle (ISA) elevations for the four most prominent and well-studied terrace levels (Figure 2). We calculated rock uplift from the measured terrace ISA elevations,

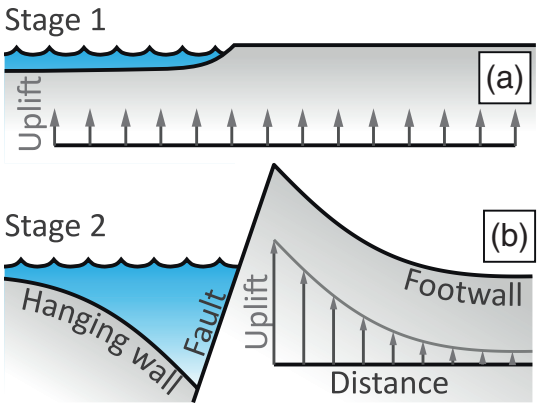

Figure 3. Simplified two-steps uplift history of the footwall across the Corinth Rift southern margin. (a) Initial, uniform uplift pattern. (b) Flexural pattern of footwall uplift after master fault (CFS) initiation.

the estimated ages, and the sea-level elevation at the time of terrace formation, as reported by de Gelder et al. (2019) (see Table S1 for marine terrace data). We determined total rock uplift since terrace formation and uplift rate. We calculate rock uplift by subtracting the modern terrace elevation from sea level elevation at the time of terrace formation, and divide this value by the terrace age to obtain uplift rate. We use a Monte Carlo routine to determine uncertainties in both calculations Figures (2c and 2d).

3.2. Forward Models

Below we describe the two models used in our study, a tectonic model that defines the spatial and temporal history of rock uplift, which is also used to approximate rock uplift recorded by marine terraces, and a geomorphic model that determines the evolution of fluvial topography.

3.2.1. Tectonic Model—From Regional to Flexural Uplift

Our tectonic model is based on the recent geological history of Corinth reviewed above, and assumes a simple two-stage uplift history: an initial period of spatially uniform regional (block) uplift, followed by a period of flexural uplift associated with a normal fault (Figure 3). The second phase of uplift in our model assumes that uplift rates vary spatially only with respect to distance from the modern fault trace and do not vary along strike, despite reported evidence (Fernández-Blanco et al., 2020). The simplified model set up acts to capture the first-order across-strike uplift history of the southern rift margin during the Quaternary (Armijo et al., 1996; de Gelder et al., 2019).

The first phase of regional uplift is modeled with a single, spatially uniform uplift rate (Figure 3a). The second phase of flexural uplift is described by analytical solutions for flexure of a broken plate (Figure 3b; Nadai, 1963):

$$U(d) = U_f \exp\left(-\frac{d}{\lambda}\right)\cos\left(\frac{d}{\lambda}\right) \tag{7}$$

where d is the distance from the broken segment, here defined as the trace of the CFS, U_f is the uplift rate at the fault, and λ is the flexural parameter defined as:

$$\lambda = \left(\frac{\mathrm{E}T_e^{\,3}}{3(\rho_m - \rho_c)g(1-\nu^2)}\right)^{1/4} \tag{8}$$

where E is Young's modulus, T_e is the effective elastic thickness of the lithosphere, ρ_m and ρ_c are the mantle and the crustal density, respectively, g is the acceleration due to gravity, and ν is Poisson's ratio. We assume standard values for E, ρ_m, ρ_c, and ν that are listed in Table 1, leaving four unknown parameters in our tectonic model: the initial block uplift rate U_i, the final uplift rate at the fault trace U_f, the effective elastic thickness of the lithosphere T_e, and the timing that flexural uplift initiated t_{int}. When the flexural rigidity is low, uplift rate in this model can go slightly negative at some distance from the fault. In our modeling, if values go negative, we set them to zero to avoid potential issues with the geomorphic forward model. This is justified by studies that report slow amounts of regional uplift not accounted for in our modeling (e.g., Turner et al., 2010). However, for thoroughness, we conducted several inversions without the positive uplift condition that are briefly discussed in the results section and presented in full in the supporting information.

To simulate modeled marine terrace rock uplift at the end of a given model run, we calculate the cumulative amount of rock uplift for each modeled terrace by integrating the modeled uplift history over a duration equivalent to the age of the observed terraces. If the terrace age is older than the transition from block uplift to flexural uplift that is set by t_{int}, it is first uplifted uniformly and then uplifted and deformed with the flexural uplift pattern. The total amount of uplift is then compared to the total rock uplift calculated for each terrace based on the terrace age, its current elevation, and the elevation of sea level at the time of terrace formation (Figure 2c).

Table 1
List of Parameters Used in the Inverse Model with Assigned Values or Range of Priors

Symbol	Description	Units	Units used in model	Value (scalar) or priors (range)
		Tectonic model		
E	Young's modulus	$M\ L^{-1}\ T^{-2}$	$kg\ m^{-1}\ yr^{-2}$	7×10^{10}
ρ_m	Density of the mantle	$M\ L^{-3}$	$kg\ m^{-3}$	3,300
ρ_c	Density of the crust	$M\ L^{-3}$	$kg\ m^{-3}$	2,700
g	Acceleration due to gravity	$L\ T^{-2}$	$m\ s^{-2}$	9.81
Te	Effective elastic thickness	L	m	1,000–10,000
v	Poisson's ratio			0.25
λ	Flexural parameter	L	m	*Calculated*
U_i	Initial block uplift rate	$L\ T^{-1}$	$m\ yr^{-1}$	1×10^{-4}–5×10^{-4}
U_f	Final uplift rate at fault	$L\ T^{-1}$	$m\ yr^{-1}$	5×10^{-4}–3×10^{-3}
t_{int}	Initiation of flexural uplift	T	yr	5×10^{5}–1.5×10^{6}
		Stream power model		
K	Erodibility	$M^{1-2\,m}\ T^{-1}$	$m^{1-2\,m}\ yr^{-1}$	1×10^{-9}–1×10^{-4}
A	Upstream drainage area	L^2	m^2	*Calculated*
S	Local channel slope			*Calculated*
m	Drainage area exponent			0.1–20
n	Slope exponent			0.5–20
E	Incision rate	$L\ T^{-1}$	$m\ yr^{-1}$	*Calculated*

3.2.2. Geomorphic Model—The Stream Power Model

We use the detachment-limited stream power model (Howard, 1994; Howard & Kerby, 1983; Whipple & Tucker, 1999) to simulate the evolution of fluvial topography through time. We combine the tectonic model with the stream power model in Equation 3 in a continuity equation to describe the evolution of the river network elevation, z:

$$\frac{dz}{dt} = U\left(x,t\right) - KA\left(x\right)^m S\left(x,t\right)^n \tag{9}$$

In this model, U is determined as a function of space (x) and time (t) based on our two-stage tectonic model described above, and A is calculated based on the modern river network derived from the DEM and assumed to be fixed in time. There are three unknown parameters, K, m, and n, and we assume that each is spatially uniform and does not change in time (see Section 3.2.3 for further discussion regarding these and other assumptions). S is also technically unknown, but it is calculated based on assumed and unknown parameters. We note that by calibrating this forward model as done here, the derived values of K, m, and n are entirely empirical and do not necessarily reflect the process-based stream power parameters used in studies such as Whipple et al. (2000) and Lague (2014) (cf. Gasparini & Brandon, 2011).

The Bayesian inverse method adopted here requires hundreds of thousands to millions of iterations to converge on a solution. To reduce computational time, we solve Equation 9 using the implicit finite difference scheme of Braun and Willett (2013), which is stable with large timesteps, with a timestep of 25,000 years. Such a large timestep introduces some inaccuracies in modeling the transient river profile evolution because the Courant-Friedrichs-Lewy condition for knickpoint propagation is not completely satisfied (Braun & Willett, 2013). However, the average errors associated with this large of a timestep are <10 m (Figure S2). We further assess the impact of the forward model step sizes by inverting a series of forward models generated with known parameters that are summarized in Section 3.2.4 and detailed in the supporting information.

For each model run, we select a suite of unknown parameter values and use them to generate an initial river profile assuming a steady-state with the initial block uplift rate. We then impose flexural uplift and let the

Table 2
Summary and Primary Model Assumptions and Their Justifications

Assumption	Justification
1. Simple two-stage uplift history	There is compelling evidence for protracted slow uplift rates prior to initiation of the modern master fault, but uplift was likely spatially variable (e.g., Ford et al., 2016). After initiation of the present-day master fault, rock uplift in the footwall has been dominated by flexure (Armijo et al., 1996; de Gelder et al., 2019; Fernández-Blanco et al., 2019, 2020)
2. Isostatic rebound due to erosion is negligible	Although not entirely correct, this is not a bad approximation, given fast extension rates of ~10 mm yr^{-1} (Avallone et al., 2004; Billiris et al., 1991) and comparatively low basin average erosion rates between 0.1 and 0.55 mm yr^{-1} (Pechlivanidou et al., 2019; Watkins et al., 2018)
3. Spatially and temporally uniform erodibility	The analysis is restricted to a single geologic unit, inside which there is little topographic evidence of strong changes in erodibility or large spatial variation in mean annual precipitation (Figures 1 and S1). Temporal variations in erodibility are difficult to vet, but several paleoclimate studies suggest a relatively steady climate in this region over the late Quaternary (e.g., Watkins et al., 2018). Without additional evidence, we make the simplifying assumption of temporally constant erodibility, but acknowledge this is a limitation of our approach
4. Fixed drainage area	Drainage divides in the area likely undergo some mobility as evidence by windgaps (Seger & Alexander, 1994; Zelilidis, 2000). In an effort to reduce the impact of divide motion, we restrict our analysis to large drainage areas (≥5 km^2)
5. Sea level fluctuations	Previous studies and our own modeling (Figure S4) show that sea level variations will result in second-order noise in river profile evolution (even under "extreme" circumstances), but that the first-order tectonic signals of interest will remain preserved in river profiles

river profile evolve according to Equation 9 for a time duration determined by t_{int}. Because flexural uplift can back tilt a river due to more rapid rock uplift toward the outlet (e.g., Fernández-Blanco et al., 2020), we impose a condition that forces the river profile to maintain a consistent flow direction to the outlet. This condition is conceptually similar to valley aggradation. For simplicity, we do not change erodibility in this segment of the modeled profile. We assess the quality of the model fit by comparing the resultant modeled fluvial topography to the observed fluvial topography.

We use the best-fit parameters recovered from the inversion to run forward models that predict sediment flux and erosion rates from each basin for comparison with data from Corinth. To predict these values from our one-dimensional incision model, we assume complete coupling between the river channel and adjacent hillslopes. This assumption allows us to assign erosion rates and determine sediment production at the catchment scale. We calculate the sediment production rate for each node in the river channel as the product of the local erosion rate and the difference in drainage area between that node and the next node upstream. These values are summed to determine sediment flux per unit time, and averaged, after weighing for drainage area, to calculate catchment average erosion rates at each time step in the model.

3.2.3. Modeling Assumptions

It is important to acknowledge and justify a number of assumptions that go into our forward model: (1) a simple two-stage uplift history described by initial block uplift followed by flexural uplift along the CFS where rivers are in steady-state with the initial uplift conditions and transiently evolve to the imposed signal of flexural uplift; (2) isostatic rebound due to erosional unloading is negligible; (3) spatially and temporally uniform erodibility; (4) fixed drainage area for each basin, and (5) sea-level fluctuations have little impact on river profile evolution. For thoroughness, we discuss our primary assumptions in detail below and list them in Table 2, along with summaries of our rationalizations and justifications of a given assumption. We readily acknowledge that the natural system is not a perfect “sandbox” experiment, and we have worked to reduce the number of complicating factors to ensure that the assumptions needed for this exercise are reasonably well justified. Moreover, should these assumptions be inaccurate or incorrect, the best-fit model residuals will exhibit systematic patterns that can be evaluated in the context of a given assumption. In addition to the justifications given below, we return to the validity of some assumptions in the discussion of the modeling results. We also emphasize that we are working with a relatively simple geomorphic model, the detachment-limited stream power incision model, and we readily acknowledge its limitations. Howev-

er, we choose this model for its widespread use in studies of bedrock channels, river profile analysis, and landscape evolution modeling.

3.2.3.1. Simple Two-Stage Uplift History

Our assumption of a two-stage uplift history is based on the previous work in the Corinth Rift that indicates a period of slow and steady uplift before the initiation of the CFS, and flexural uplift of the southern footwall thereafter (Armijo et al., 1996; Bell, 2008; de Gelder et al., 2019; Fernández-Blanco et al., 2019; Gawthrope et al., 2017). It is difficult to reconstruct the earlier uplift history in space and time, but previous studies indicate that the crust was slowly extending (extension rates = 1 mm yr^{-1}) (Ford et al., 2013) along several normal faults (e.g., Gawthrope et al., 2017; Ori, 1989). These results suggest that the assumption of spatially uniform uplift is not entirely correct. While imperfect, we still consider that it is a decent first-order approximation over the relatively-small length scales of the river systems considered here (<50 km). We further assume that the river profiles are in steady-state with this initial block uplift field. This is a necessary simplification to perform the inverse modeling exercise because there is little information available to otherwise reconstruct the paleotopography needed to constrain the initial condition.

Flexural uplift after the onset of the CFS is an assumption that is easier to justify, based on the previous studies of deformed marine terraces and fluvial systems within the study area that are described in detail above (Armijo et al., 1996; de Gelder et al., 2019; Fernández Blanco et al., 2019, 2020). While there are some subsidiary normal faults south of the main fault, they are inactive, or at most, their activity is low and offsets small, such that the approximation of a single rift bounding fault is reasonably appropriate (e.g., Bell et al., 2017; de Gelder et al., 2019). Furthermore, it is clear from the deformed marine terraces that the dominant direction of variability in uplift rate is perpendicular to the fault strike (Armijo et al., 1996; de Gelder et al., 2019). However, as noted by Fernández-Blanco et al. (2019, 2020) and consistent with mechanical models for fault growth, there is a long-strike variability in the footwall uplift rate associated with fault growth and propagation. We neglect along-strike variations, owing to the relatively small along-strike dimension of our study area (~20 km). This inference is supported by an analysis of residuals between observed and modeled terrace elevations (conducted by fitting Equations 7 and 8 to the marine terraces) that shows no systematic along-strike variation (Figure S3).

3.2.3.2. Isostatic Rebound due to Erosion is Negligible

The lithosphere will rebound isostatically due to erosional unloading, and this signal will be dampened and modified by the rigidity of the lithospheric plate (Watts, 2001). In the case of Corinth, this effect is likely to be small relative to the tectonically induced uplift. High extension rates, ~15–10 mm yr^{-1} (Avallone et al., 2004; Billiris et al., 1991) result in fast footwall uplift rates, >1.5 mm yr^{-1} (Armijo et al., 1996; de Gelder et al., 2019). Basin average erosion rates derived from the sedimentary record in Corinth are on the order of 0.10–0.55 mm yr^{-1} with most < 0.30 mm yr^{-1} (Pechlivanidou et al., 2019; Watkins et al. 2018), such that erosional rebound is only a fraction of the total footwall uplift rate. The tectonic rates, thus, dominate footwall uplift in the Corinth Rift margin, with erosion playing only a minor role, suggesting that this simplifying assumption is reasonable.

3.2.3.3. Spatially and Temporally Uniform Erodibility

In an attempt to best ensure spatially uniform erodibility, we restrict our analysis to a single geology unit, which consists of a package of interbedded marl, siltstone, sandstone, conglomerate, and conglomeratic fan deltas. Obviously, this unit is not homogenous, but over the length scales considered, the heterogeneity is probably small and likely negligible. This assertion is supported by river profiles and hillslope gradient maps that do not show distinct stepped morphologies (beyond those artifacts in the DEM) that are commonly observed in horizontal or subhorizontal strata with strong differences in erodibility (Figures 2e and S1). Furthermore, several other geomorphic studies assume that comparable units within Corinth maintain spatially and temporally uniform erodibility and generate results that mimic geological observations (Pechlivanidou et al., 2019; Watkins et al., 2018; Zondervan et al., 2020). As noted above, there are small amounts of valley aggradation upstream in the river network associated with back tilting due to flexural uplift (Fernández-Blanco et al., 2020), but such deposits are spatially limited. We make the simplifying assumption that these units do not significantly affect channel erodibility in our model, but recognize this is a limitation of

our approach. Spatial variations in rainfall might also affect erodibility as cast here, but mean annual precipitation shows only minor differences throughout the study area (Figure S1; Hijmans et al., 2005).

It is difficult to evaluate the assumption of temporally invariant erodibility, which would presumably be mainly related to climate-induced changes in discharge and sediment supply. Regional climate in the study area has remained relatively consistent over the last ~130 ka, despite large swings in global climate (Watkins et al., 2018). The proxies and models used to demonstrate relatively stable climate are not sensitive to, or do not consider, potentially important climatic variables, such as storminess; however, Watkins et al. (2018) suggested climate variations since 130 ka resulted in temporal variations in sediment flux on the order of 10%–20%. Nonetheless, due to the absence of records preceding this period, and to simplify our analysis, we assume that erodibility has been temporally constant in the study are over the duration recorded by the river systems. While somewhat limiting, we note that Pechlivanidou et al. (2019) made a similar assumption and was able to reproduce geological observables using the stream power model in Corinth.

3.2.3.4. Fixed Drainage Area

Considering the active nature of the tectonics and geomorphology in Corinth, it is likely that there is some lateral movement of drainage divides in the study area. For example, drainage divides might be slowly migrating in response to footwall tilting. Studies of topography and stratigraphy show evidence of past river capture events, and the two most westward basins in the study area preserve windgaps along present-day southern-most divides, which are indicative of drainage area exchange (Seger & Alexander, 1994; Zelilidis, 2000). However, given the difficulty of reconstructing the initial drainage basin size and divide motion history, we make the simplifying assumption of static drainage networks to make the inverse problem tractable.

Whipple et al. (2017) showed that typically river response times are much faster than divide migration rates, such that rivers can remain faithful recorders of tectonic activity in conditions with slow and steady divide migration. Nonetheless, we recognize the evidence of divide migration from the geologic record needs to be considered, as past drainage area exchange can affect the inverse modeling of river profiles. Such effects are most pronounced at low drainage areas near the moving divide, given that the impact of drainage area gain or loss on a particular point in the river profile is proportional to the ratio of the area gained or lost relative to the drainage area at that specific point (Whipple et al., 2017). Thus, the channel reaches with larger drainage area are less affected compared to those with smaller drainage area. Based on these considerations, we attempt to minimize the effects of drainage area exchange by using a relatively large drainage area of 5 km^2 to define our river networks.

3.2.3.5. Sea Level Fluctuations

Previous studies show that sea level rise and fall affect river profiles if the base level fall signal can propagate upstream to higher elevations faster than a subsequent sea level rise. This effect is maximized in highly erodible rocks, at low uplift rates, and with gently sloping coastlines (Snyder et al., 2002). In the case of Corinth, while previous studies suggest rocks flooring the rivers in the studied basin are relatively erodible (Zondervan et al., 2020), the uplift rates are extremely rapid, and the coastline is bound by a steep fault scarp or steep shelf, suggesting that the river profile might be spared the effects of sea level fluctuations. This assumption is supported by river profiles that do not preserve evidence of multiple knickpoints associated with sea-level change and river channels that are primarily cut into bedrock, rather than alluviated, along most of the river length (Figure 2e).

To further evaluate this assumption, we ran simulations with the stream power incision model, sea level variations inspired by Milankovitch periodicities, and a simple one-dimensional wave-cut platform model (Anderson et al., 1999; Snyder et al., 2002). The results, presented in the Supporting Information for brevity (Figure S4), show that sea level fluctuations have minimal impact on the first-order characteristics of river profile evolution, even with erodible rocks and high rates of wave cutting. This model set up is designed to amplify a sea level signal, and in reality, this signal is buffered by alluviation in lower reaches. This process is not included in our inverse models, which is why we exclude the lower alluviated potions of the channels from our analysis. Collectively, this exercise suggests that our simplifying assumption of static sea level is a reasonable approximation.

3.2.4. Inverse Model

We adopt a Bayesian framework to invert for seven unknown parameters (four tectonic—the initial uplift rate, U_i, the final uplift rate at the fault, U_f, the fault initiation time, t_{int}, and the effective elastic thickness, T_e, and three geomorphic—the erodibility, K, the drainage area exponent, m, and the slope exponent, n) in our forward model. We chose Bayesian inference for its flexibility in nonlinear inverse problems. Bayes' theorem states that the probability of the model, M, given the data, d, which is known as the posterior probability distribution or more simply the posterior, $P(M|d)$, is proportional to the product of the likelihood of the data given the model, $P(d|M)$, and the probability of the model, which is known as the prior probability distribution function or more simply the prior, $P(M)$, of the model (Bayes & Price, 1763):

$$P\left(M \mid d\right) \propto P\left(d \mid M\right)P\left(M\right) \tag{10}$$

We use a Markov chain Monte Carlo (MCMC) routine using the Metropolis-Hastings algorithm to populate the posterior probability distribution (Aster et al., 2019; Metropolis et al., 1953). This approach works by drawing a suite of parameter values based on a prescribed prior distribution using a random walk of a given step size and then using those parameters to run a forward model to compare the model result to the data using a likelihood function. In this case, we use so-called "uninformative" priors that are drawn from a broad parameter range with uniform probability. The prior ranges in our study are based on knowledge of the geological history of the study area and parameter values reported elsewhere. Table 1 lists the prior probability ranges for the seven free parameters in the forward model used in our inversion. We also ran several models with wider priors for the erodibility that range from 1×10^{-80} to 1×10^{-4} $\text{m}^{1-2\,\text{m}}$ yr^{-1}. This analysis is presented in the supporting information and was conducted for two reasons. First, as noted above, K is dependent on m and n and our wide range of priors for m and n permits such a wide range of K, and, second, it allowed us to explore the sensitivity to priors on inverse model convergence.

The Gaussian-likelihood function is a common choice to determine the posterior and is the product of the variance-weighted squared residual. The log-likelihood is often used to avoid issues with precision associated with taking the product of very small numbers, and is the likelihood function that we use in our simulations where:

$$\log\left(P\left(d \mid m\right)\right) \propto -\frac{1}{2}\sum_{i=1}^{m}\left(o_i - e_i\right)^2 / \sigma_i^2 \tag{11}$$

where o is the observed data, e is the corresponding expected or modeled value, and σ is the uncertainty represented as the standard deviation (Aster et al., 2019). Vertical uncertainties on the DEM used to extract the river profile data are typically on the order of several meters, and here we assign errors of 5 m (25% of the horizontal resolution) to each data point. For the marine terraces, we incorporate uncertainties in the measured elevation, the elevation of sea level at the time of terrace formation, and the terrace age using a Monte Carlo routine to determine total rock uplift since terrace formation (Figures 2b, 2c, and 2d; Table S1).

Our inversion uses two different data sets to define the posterior distributions of the seven free parameters: longitudinal river profile elevations and the total rock uplift derived from each marine terrace. Based on the equation above, each data point is treated equally with respect to its given uncertainty. As such, the river profiles will influence the inversion more strongly than marine terraces simply because there are more river profile data points (n = 7,195) than marine terrace data points (n = 297). Since there is no reason to think that the river profile data are an order of magnitude more important than the marine terrace data, we impose a weighting such that both data sets are considered equally in our likelihood function.

To ensure convergence of the MCMC on the posterior, we ran 15 individual chains with 3.3 million iterations each. Each of the 15 chains took approximately 21 days or ~500 computational hours on a single Intel Xeon E5-2680 v3 core to complete the more than three million model iterations. Chains were initially started randomly within the prior probability range, but due to slow convergence into the optimal parameter space, a common issue with the Metropolis-Hastings sampler, we selected initial parameter values randomly from a smaller range about the maximum a posteriori (MAP) solution, which represents the most likely or best-fit solution, from the preceding Markov chains. The random walk step size was manually adjusted

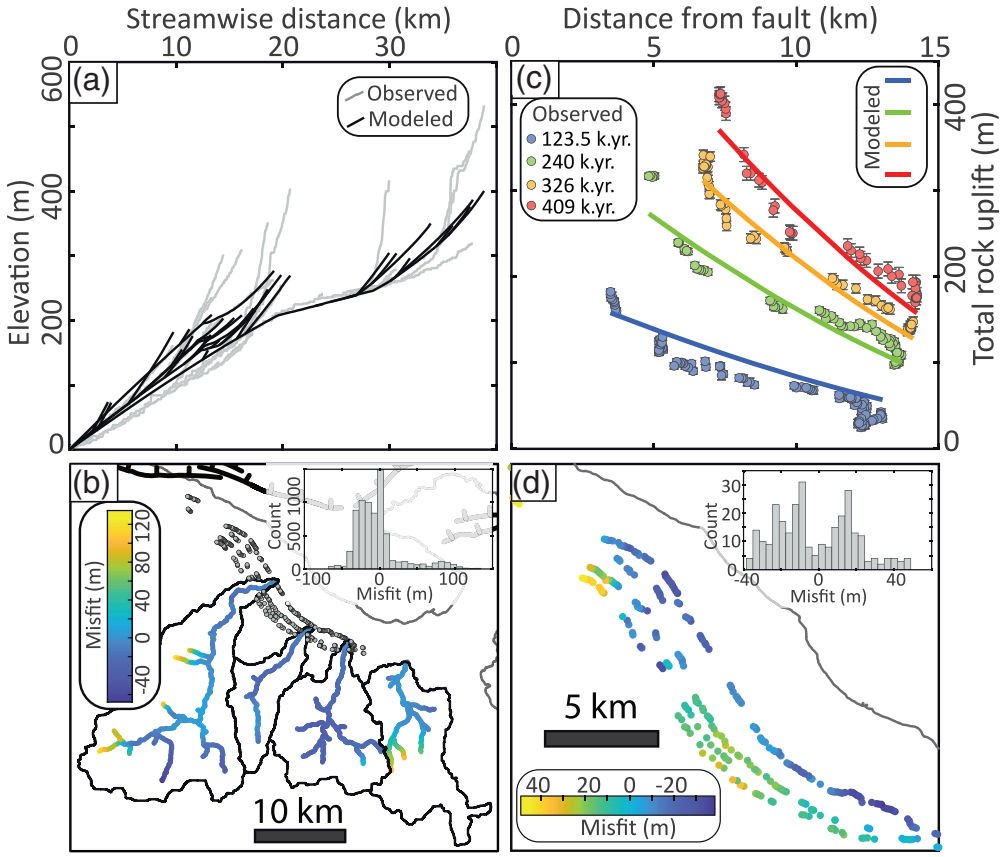

Figure 4. Observed versus best-fit model data. (a) Observed and modeled river profiles. Note that the observed and modeled river profiles from all four basins are shown in this figure. (b) Map view of the misfit between observed and modeled river profile elevations, with a histogram of the misfits (inset). (c) Observed and model marine terrace elevations plotted as a function of Euclidean distance normal to the master fault. The average age of each terrace is noted in the legend. (d) Map view of the misfit between observed and modeled marine terrace elevations with a histogram of the misfits (inset).

to achieve acceptance ratios between ~20% and 50%, with most chains having an acceptance ratio of ~40%, which suggests the MCMC is optimally tuned (Gelman et al., 2013). The burn-in period is the time it takes the chain to converge on the optimal solution region in the multi-dimensional space, which here typically consisted of 300,000 iterations and was discarded before generating the posterior. We did not include two chains into our population of the posterior distributions; one chain that did not converge into the high likelihood zone and another chain that demonstrated slow convergence, finding the high likelihood region after ~1 million iterations (Figure S5). After discarding the burn-in, the posterior was generated by thinning to avoiding autocorrelation by selecting every 1,000th model of each of the remaining 13 chains. The parameters from this thinned population were then used to quantify the posterior probability distribution for each of the seven parameters in our forward model.

We ran a series of simulations to test the inverse model and evaluate the impact of the time step size chosen in the forward models. We use a short time step (100 yr) to generate simple transient river profiles and synthetic "marine terraces" with known parameters. We then invert the known models using the Bayesian scheme outlined above with forward model timesteps of 1, 10, and 25 kyr (and detailed in the supporting information). The Bayesian inversion recovers model parameters well. The distribution of model posteriors contains the true solution in all cases, regardless of the time step size chosen for the forward model (Figures S6, S7, and S8). For most cases and parameters, the MAP solution is near the true solution. One exception occurs when $n = 1$ in the true solution, where there is a systematic drift of K and the initial uplift rate with the chosen forward model step size. This analysis gives confidence the inversion method can recover model parameters reasonably with the large timestep size used here.

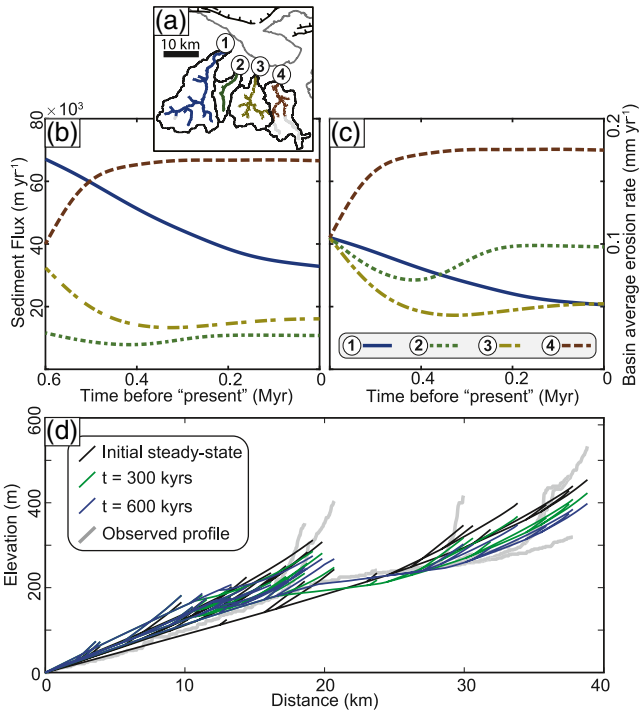

Figure 5. Forward model predictions determined using the best-fit (MAP) solution. (a) Drainage basins and river networks used in the forward model, where the river network of each basin is colored differently. (b) Sediment flux and (c) basin average erosion rate for each drainage basin run over a 600 kyr period and colored according to the associated river networks shown in (a). Note the variable response of each basin. (d) Modeled river profile evolution in three timesteps with the observed profiles in the gray for reference. This simulation shows only the largest drainage basin to simplify the presentation of the results.

4. Results

4.1. Model Fits and Forward Model Predictions

The MAP or best-fit solution fits both the river profiles and marine terraces well (Figure 4). The best-fit tectonic parameters are $U_i = 0.105$ mm yr^{-1}, $U_f = 1.64$ mm yr^{-1}, $t_{int} = 598$ kyrs, and $T_e = 2.35$ km, and the best-fit geomorphic parameters are $K \approx 1.45 \times 10^{-7}$ m$^{1-2\,m}$ yr^{-1}, $m = 2.04$, and $n = 6.98$. The river profile elevation residuals range from ~−120 to 60 m and define a right-skewed distribution with a mean ± 1σ of -3 ± 31 m and a median of ~-8 m (Figures 4a and 4b). The largest misfits occur at high elevations and low drainage areas near the channel network heads, and moderate misfits exist along the knickzones (Figures 4a and 4b). The inversion favors the data-dense areas spanning the knickzones over the data-sparse regions near channel heads, which represent only < 5% of the fluvial channel data set. This leads to high residuals near channel heads (Figure 4c). However, recognizing that these misfits are important in interpreting our results, we discuss them in detail in Section 5.2.3.2.2. The residuals for the marine terraces have a range of approximately ± 50 m about a mean of -2 ± 20 m with a median value of ~-7 m (Figures 4c and 4d). The highest misfits are noted for terraces closest to the fault; moderate positive and negative misfits are generally observed at intermediate and long distances from the fault, respectively (Figures 4c and 4d).

The results from the best-fit forward model predict sediment flux that ranges from 1.5 to 67 × 10^3 m^3 yr^{-1} and catchment average erosion rates between 0.04 and 0.18 mm yr^{-1} (Figures 5a, 5b, and 5c). The model results also show a variable sediment flux and erosional response among the four studied catchments (Figures 5a, 5b, and 5c). Three of the basins show reductions in sediment flux and erosion rate in response to flexural uplift, and the easternmost basin exhibits an increase.

We also use the forward models to explore the evolution of fluvial topography in the Corinth Rift footwall using the best-fit parameters. We run a model for the longitudinal profile of the Asopos River (River 1), the largest drainage basin in our study area (Figures 1b and 5d). Despite a substantial change in the spatial and temporal pattern of rock uplift, total fluvial relief remains approximately constant. The river profile generates a large knickpoint, and fluvial relief increases slightly downstream of the knickpoint, in the lower ~15 km of the river network, yet, a small decrease in relief is observed in the headwaters (Figure 5d). Note that while the rock uplift becomes spatially variable after fault initiation, the mean uplift rate of the basins does not change substantially and actually declines in some basins (cf. Figure 5c).

4.2. Parameter Values and Posterior Distributions

All of the parameter posterior distributions define narrow regions within the wide range of the priors (Figures 6 and S5, Tables 1 and 3). Interestingly, despite the tight distributions, the MCMC finds a bimodal distribution of acceptable models in the parameter space. One posterior mode is narrower with a slightly higher likelihood and contains the MAP solution. The other high-likelihood zone is wider, with a marginally lower likelihood that is sampled more by the MCMC (Figures 6 and S5).

For the tectonic parameters, T_e and U_f are largely determined by the marine terrace data and have very tight distributions about means of 2.37 km and 1.63 mm yr^{-1}, respectively, and MAP values of 2.35 km and 1.64 mm yr^{-1}, respectively (Figure 6, Table 3). The timing of the transition from block uplift to flexural uplift (t_{int}) and U_i are entirely determined by the river profiles because they record information from a time before the construction of the oldest terrace. The posterior distributions for t_{int} and U_i are wider, with mean values of 560 kyr and 0.13 mm yr^{-1}, respectively, and MAP values of 598 kyr and 0.105 mm yr^{-1}, respectively (Figure 6 and Table 3).

Table 3
Summary of Inverse and Forward Model Results and Parameter Values Reported in the Literature

Parameter name	Parameter symbols and units	Value in this study (MAP[a] solution [range[b]])	Values in other studies	Key references
Initial uplift rate	U_i (mm yr^{-1})	0.105 [0.1–0.2]	0–0.3	Armijo et al. (1996) and Turner et al. (2010)
Final uplift rate at the fault	U_f (mm yr^{-1})	1.64 [1.60–1.66]	1.6–1.7	Armijo et al. (1996) and de Gelder et al. (2019)
CFS initiation time in the Eastern Sector	t_{int} (kyrs)	598 [500–663]	600–2,000	Armijo et al. (1996), Brasier et al. (2011), de Gelder et al. (2019), Ford et al. (2007, 2017), Nixon et al. (2016), and Rohais et al. (2007)
Effective elastic thickness	T_e (km)	2.35 [2.32–2.42]	2.0–2.5	Armijo et al. (1996)
Erodibility constant (general)[c]	K (m$^{1-2\,m}$ yr^{-1})	$1 \times 10^{-6.84}$ [$1 \times 10^{-7.39}$–$1 \times 10^{-5.71}$]	1×10^{-3}–1×10^{-7}	Stock and Montgomery (1999)
Erodibility constant (Corinth)[d]	K (m$^{1-2\,m}$ yr^{-1})	N/A [1.6×10^{-6}–6.2×10^{-6}]	~1.5×10^{-6}–6×10^{-6}	Pechlivanidou et al. (2019) and Zondervan et al. (2020)
Drainage area exponent[e]	m	2.04 [1.57–2.16]	~0.25–3	Harel et al. (2016) and Lague (2014)
Slope exponent[f]	n	6.98 [5.20–7.40]	~0.5–6	Harel et al. (2016) and Lague (2014)
Sediment flux[g]	N/A (m^3 yr^{-1})	1.5–67 $\times 10^3$	~1–80 $\times 10^3$	Pechlivanidou et al. (2019) and Watkins et al. (2018)
Erosion rate[h]	N/A (mm yr^{-1})	0.04–0.18	~0.1–0.55	Pechlivanidou et al. (2019) and Watkins et al. (2018)

[a]MAP – maximum a posteriori. [b]Our reported range of values recovered from the inversion posterior. Note that this range is much smaller than the prior ranges presented in Table 1 highlighting the narrow range of the optimal parameter space. [c]Our reported values are relative to our recovered m and n values. These from Stock and Montgomery (1999) are the reported range from their analysis of globally distributed streams. [d]Erodibility from our values assuming $m = 0.5$ and $n = 1$ for comparison with the cited studies. See text for details on this conversion. [e]Range of values shown is for typically reported values. [f]Range of values shown is for typically reported values. [g]Values not solved for inversion but derived from MAP solution from the inversion. [h]Values not solved for inversion but derived from MAP solution from the inversion.

The geomorphic parameters strike a balance between fitting the uplift history defined by the marine terraces and the transient morphology of the river profiles. The mean and MAP value for the erodibility constant, K, are ~3.98×10^{-7} m$^{1-2\,m}$ yr^{-1} and ~1.45×10^{-7} m$^{1-2\,m}$ yr^{-1}, respectively. Mean and MAP values for m and n are 1.88 and 2.04, and 6.43 and 6.98, respectively (Figure 6 and Table 3).

The parameters show some interesting tradeoffs and covariance. Values of m and n, show a strong linear covariation with a consistent ratio of 0.3 (Figure 6); recall that the ratio of m to n is the river profile concavity, θ. This value is on the lower end of typically observed river profile concavity, but it is consistent with the concavity for the studied rivers in Corinth calculated using traditional slope-area and χ analysis. There is also a strong linear covariation between both m and n and U_i and a nonlinear correlation with these parameters and K (Figure 6). Linear covariation is also observed between U_f and T_e, and U_f and t_{int} (Figure 6). Nonlinear covariation is noted between U_i and K (Figure 6). All other parameters appear weakly correlated or uncorrelated (Figure 6). We note that these results are generally consistent with other inverse model results, presented in the Supporting Information, that allow for (1) wider priors on the erodibility constant (Figure S9) and (2) models that allow the flexed uplift pattern to go negative (Figure S10). These findings indicate that the inversion results are robust.

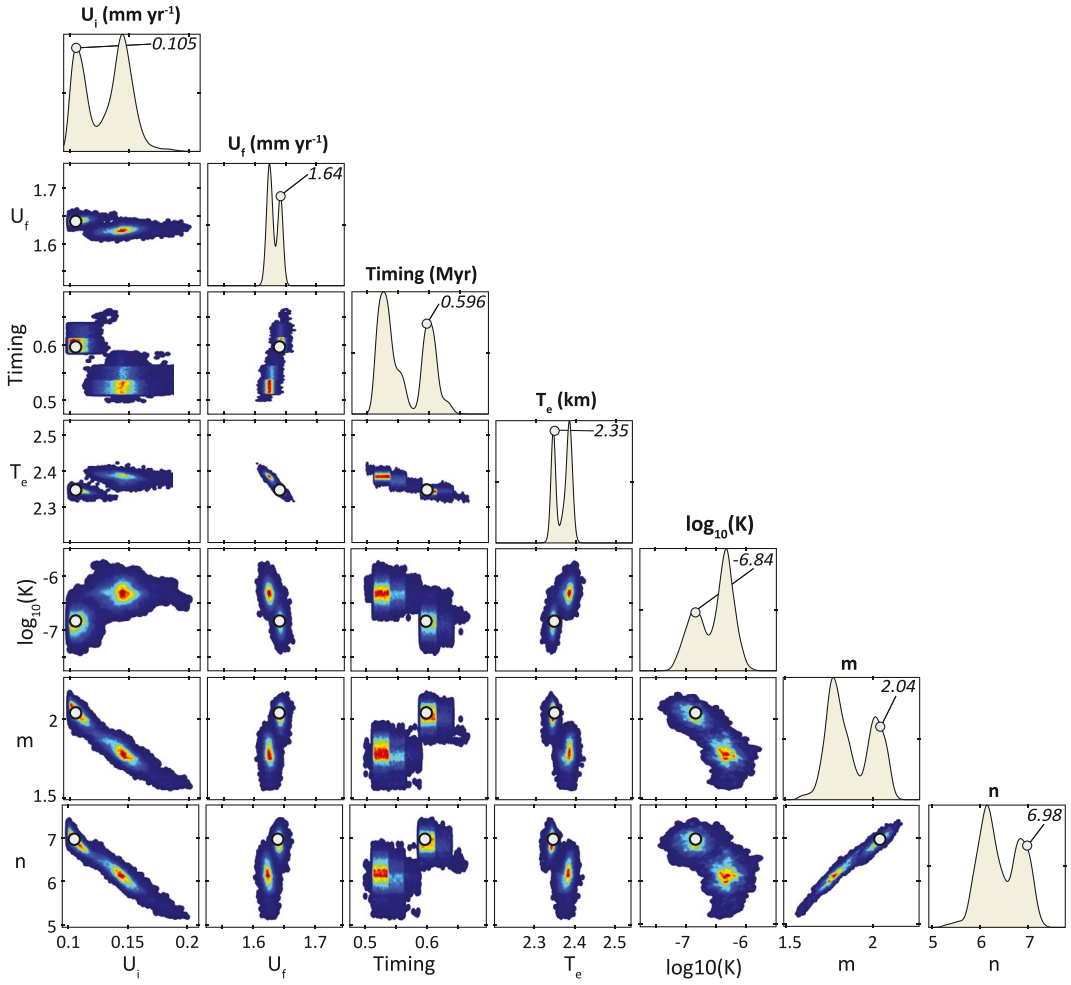

Figure 6. Matrix plot of the posterior probability distributions from the Markov chain Monte Carlo inversion. The bivariant plots show the two-dimensional probabilities between parameters that highlight their covariance with one another. The maximum a posteriori (MAP) solution for each parameter is noted by the gray dot, and the parameter value is given in the upper-right corner of each upper diagonal plot, which shows the relative marginal posteriors associated with each model parameter.

5. Discussion

5.1. Tectonic Parameters

Parameters resolved for the tectonic model are consistent with results from previous studies. This finding is perhaps not surprising for the final uplift rate at the fault trace, $U_f = 1.64$ mm yr^{-1}, and for the effective elastic thickness, $T_e = 2.35$ km, for they both rely heavily on the marine terrace data that is also used for previous estimates. Using the same terrace sequence as this study and a finite element model for rift development, both Armijo et al. (1996) and de Gelder et al. (2019) estimate maximum footwall uplift rates of ~1.6–1.7 mm yr^{-1}. Armijo et al. (1996) also recovered a rigid layer thickness of ~10 km, which translates into a T_e between 2.0 and 2.5 km, in line with our determination (Table 3). The offshore sedimentary record in the hanging wall, both from cores and geophysics, suggests similarly rapid slip rates and flexural wavelengths (de Gelder et al., 2019; McNeill et al., 2019).

Estimates of the initial rock uplift rate, $U_i = 0.105$ mm yr^{-1}, and the timing of flexural uplift onset, $t_{int} = 598$ kyr, are less well-resolved than the other two tectonic parameters, as they are almost entirely determined by the river profile elevation data. Our estimated range of U_i between 0.1 and 0.2 mm yr^{-1}, is consistent with previous studies that suggest a regionally averaged rock uplift rate of 0–0.3 mm yr^{-1} (Table 3; Armijo et al., 1996; Turner et al., 2010). The lower end of the posterior range is determined by the prior, but the

MAP solution is well within the prior range (Figure 6; Tables 1 and 3). The largest misfits between the observed and modeled profiles are noted near the channel heads (Figures 4a and 4b). As noted above, these large misfits are largely due to the fact that low drainage areas near the channel heads account for <5% of the data in the fluvial network; the inversion is strongly controlled by the data-dense region along the knickzone. However, this systematic residual pattern also highlights a number of potentially relevant processes not accounted for in our model, such as spatially variable rock uplift rate before fault initiation, drainage reorganization, or spatially variable stream power parameters (see discussion below). Nonetheless, the model fits most of the river profiles well, and the misfits are small, suggesting that our simple model acts to capture the first-order evolution of the footwall of the CFS.

The timing of fault initiation has been a topic of interest in Corinth for decades (e.g., Fernández-Blanco, 2019). Our model results suggest an onset of flexural uplift (t_{int}) between ~500 and 660 kyr ago, with a best-fit of ~600 kyr. These ages are generally younger yet overlapping with that in several previous studies (Figure 6 and Table 3). Previous age estimates range from ~2,000 to 600 kyr (Armijo et al., 1996; Brasier et al., 2011; de Gelder et al., 2019; Ford et al., 2007, 2017; Gawthorpe et al., 2017; Nixon et al., 2016; Rohais et al., 2007). Our results favor the younger end of this range for the Eastern Sector, which is consistent with interpretations of other studies (de Gelder et al., 2019; Nixon et al., 2016). Our results do not support an onset timing >~660 kyrs, but it is important to note that our modeling reflects the timing of the transition to a pure mode of rapid flexural uplift. In other words, the CFS in the Eastern Sector might have initiated earlier, and footwall uplift rates were slow and/or similar to the background rate before accelerating to contemporary rates at ~600 kyr ago.

While we consider that our t_{int} estimates are reliable, there are some factors that might bias modeled initiation times based on our assumptions and approach. Changes in drainage area through divide migration will affect discharge, and thus stream power, at a given point downstream. Such changes will alter knickpoint migration rates and the temporal scaling of the river profile. These processes are not accounted for by our model but can impact the derived initiation time of faulting; an expansion or contraction of the drainage basin would decrease or increase the calculated initiation time, respectively. The use of several drainage basins serves to reduce these effects if drainage area exchange were lateral between basins, thus buffering the impact of reorganization of a single basin. As discusses earlier, there is evidence of past drainage area exchange (Seger & Alexander, 1994; Zelilidis, 2000). We attempt to minimize these effects in our analysis by defining channel heads at relatively large drainage areas. We think the consistency between our inferred fault initiation timing and independent estimates is compelling evidence suggesting minimal impact of drainage reorganization on the inversion approach, at least at the timescales considered here.

5.2. Geomorphic Parameters

5.2.1. Comparison of Forward Model Results with Previous Studies

Sediment flux of rivers draining the gulf and basin average erosion rates along its margins are useful observables for comparison with our forward model predictions. To our knowledge, two studies have estimated sediment flux to the Gulf of Corinth since the initiation of the present-day rift bounding fault (CFS) (Pechlivanidou et al., 2019; Watkins et al., 2018). Sediment flux estimated by these studies come from the stratigraphic record and calibrated models of landscape erosion, and range from $\sim 1 \times 10^3$ to 80×10^3 m^3 yr^{-1}, with catchment average erosion rates that range between ~0.1 and 0.55 mm yr^{-1}, with most reported values <0.3 mm yr^{-1}. These studies generally focus on the Late Quaternary history of sedimentation into the gulf, and they provide an order-of-magnitude estimate on sediment flux and erosion rates since the initiation of the CFS.

Our model results of sediment flux range from 1.5×10^3 to 67×10^3 m^3 yr^{-1}, and catchment average erosion rates between 0.04 and 0.18 mm yr^{-1} (Figures 5a, 5b, and 5c) are in line with previous studies (Table 3). Again, this consistency emphasizes that the calibrated model parameters can predict geologic observables and gives confidence that the parameters recovered are reasonable. The variable sediment flux and erosional response of the basins is nevertheless a surprising outcome (Figures 5a, 5b, and 5c). The reduction in sediment flux and erosion rate in the three westernmost basins is not unexpected; the rock uplift rate decreases away from the outlet as the flexural signal reduces uplift rates relative to the initial condition,

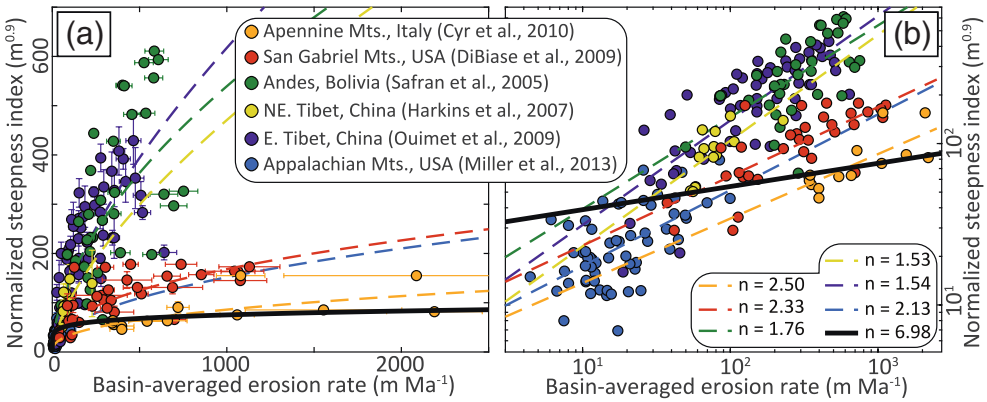

Figure 7. Basin average erosion rate (E) versus the normalized steepness index (k_{sn}). (a and b) Show a compilation of basin average erosion rates derived from measurements of the concentration of beryllium-10 in quartz-rich fluvial sands versus the basin average k_{sn} for drainage basin thought to be in steady-state (data are from Kirby & Whipple, 2012). (a) Is a linear representation of the data, and (b) is the same data with logarithmic axes. The dashed lines show the best-fit power-law regression through each data set, and the power-law exponent is noted and represents the slope exponent n in the stream power incision model. The bold black line shows the theoretical relationship between E and k_{sn} using the best-fit parameters from the inversion of the rivers in the Eastern Sector of the Corinth Rift.

and the net result of this uplift pattern is to reduce sediment flux and erosion rates. This result is consistent with that from Pechlivanidou et al. (2019). In contrast to this general pattern, the easternmost basin shows an increasing trend (Figures 5a, 5b, and 5c). This response is due to the shape of the eastern basin, which is wider near the outlet than its three western neighboring basins. This deviation in basin shape allows for a larger area to experience higher uplift rates near the fault and acts to elevate sediment flux and erosion rate from this basin.

This simulation shows that the sediment flux and erosional response of a catchment depend on the interaction between the spatial pattern of uplift and the shape of the drainage basin. These factors can result in a sediment flux response that is highly variable for adjacent catchments exposed to the same forcing. We nevertheless recognize that these models are not perfect realizations of the actual sediment flux patterns and that dynamic adjustments in basin shape are likely for drainages responding to a change in uplift rate.

The subdued topographic reaction of the river network to the change in uplift regime is also somewhat surprising (Figure 5d). Given that the uplift rate at the fault is ~1.6 mm yr^{-1}, one might expect a large increase in fluvial relief. While a modest increase in relief occurs within the knickzone, elevations in the headwaters decline. This response is mostly due to the fact that the studied basins are several kilometers away from the fault trace, and uplift rates decline exponentially away from the fault. As a result, the mean uplift rates within the basins before and after fault initiation are similar and even fall in some cases (cf. Figure 5c). However, the highly nonlinear relationship between erosion rate and channel steepness predicted by large m and n values also play a role in contributing to the muted topographic response to changes in rock uplift rate, particularly within the knickzone proximal to the fault trace. This latter finding has obvious implications for the interpretation of tectonic signals from topography, and we discuss it in detail in Section 5.2.3.

5.2.2. Erodibility (K)

Stock and Montgomery (1999) showed that the erodibility constant varies over a range of 4–5 orders of magnitude, and our results fall roughly within this broad range (Table 3). Previous studies that calibrate K in Corinth using versions of the stream power model assume that $m = 0.5$ and $n = 1$ and report values that range from $\sim 1.5 \times 10^{-6}$ to 6×10^{-6} m$^{1-2\,m}$ yr^{-1} (Pechlivanidou et al., 2019; Zondervan et al., 2020). Because the value of K is sensitive to m and n, our results are not directly comparable to these studies. For a more direct comparison, we calculate a transformed, or normalized, K based on our best-fit results assuming $m = 0.5$ and $n = 1$. For this exercise, we assume a range of uplift rates from 0.2 to 1 mm yr^{-1} and calculate the theoretical steady-state river profile using the MAP solution. We then calculate the K value needed to match the predicted fluvial relief assuming $m = 0.5$ and $n = 1$ and find a range of erodibility from $\sim 1.6 \times 10^{-6}$ to

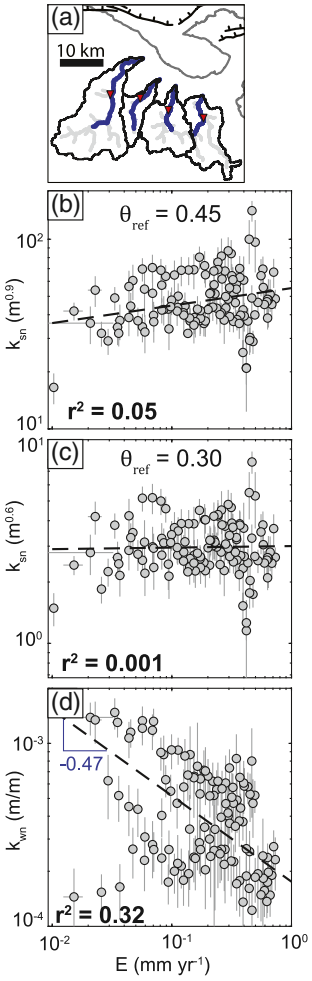

Figure 8. Normalized steepness index, k_{sn}, and normalized width index, k_{wn}, analysis for trunk channel reaches spanning the transient knickzone. (a) Map of the river network with the analyzed reaches highlighted in blue. (b and c) Show k_{sn} calculated using a reference concavity θ_{ref} of 0.45 and 0.30, respectively, in increments of 500 m streamwise distance, plotted against the best-fit model incision rate. The two different references concavities used to calculate k_{sn} are based on the commonly used value (0.45) for comparison with other studies and the best-fit value from the inverse model (0.30). (d) k_{wn} calculated every 500 m and using a reference channel wideness exponent of 0.50 plotted against the best-fit modeled incision rate.

$\sim 6.2 \times 10^{-6}$ $m^{1-2\,m}$ yr^{-1}. These results are consistent with the previously reported range of erodibility estimates known for the area for comparable rock types (Table 3; Pechlivanidou et al., 2019; Zondervan et al., 2020).

5.2.3. Drainage Area (m) and Slope (n) Exponents

While the m to n ratio recovered in this study is consistent with theory and empirical investigations, their absolute values are abnormally high relative to those from the existing literature. The m and n values for the Eastern Sector indicate a highly nonlinear scaling between channel steepness and erosion rate that predicts fluvial topography is relatively insensitive to rock uplift rates exceeding ~0.05 mm yr^{-1}. This is perhaps not an unexpected finding given that there is little change in fluvial topography (i.e., channel steepness) along the knickpoint face despite a strong gradient in rock uplift rate (Figures 2 and 4). The important implications that these parameters have for the long-term evolution of river profiles, and interpretations of tectonics drawn from fluvial topography, encourage the thorough discussion attempting to interpret these parameters that follows. Below, we place our findings in a broader context by comparing them to those from the literature to date and vet potential explanations for high m and n values for the Corinth Rift, and generally.

5.2.3.1. Comparison with Previous Studies

To our knowledge, there exist no calibrations of m and n for Corinth rivers, but the global compilations described in Section 2.6 provide some basis for comparison (Table 3). Lague (2014) showed m ranged from ~0.5 to 2 and n from ~1 to 4, and Harel et al. (2016) reported means (± 1σ) of ~1.35 (± 1.45) and ~2.7 (± 2.9) for m and n, respectively. Our best-fit m and n values of 2.04 and 6.98, respectively, are high relative to the compilations of Lague (2014) and Harel et al. (2016); for example, only 5% of the >1,200 n values reported by Harel et al. (2016) are greater than 7 (Table 3).

We highlight the unusual nature of the m and n parameters recovered from river profiles in the Eastern Sector of Corinth through a comparison with a compilation of published erosion rate and k_{sn} data for drainage basins assumed to be in steady-state (Kirby & Whipple, 2012) (Figure 7). In their analysis, Kirby and Whipple (2012) calculate k_{sn} using a m to n ratio of 0.45 for five different regions, and power-law regressions through these data indicate that m ranges from ~0.7 to 1.2 and n from ~1.5 to 2.5. Based on the best-fit stream power parameters from the Corinth Rift Eastern Sector, we simulate theoretical steady-state river profiles for a range of uplift rates from 0 to 2 mm yr^{-1} and calculate k_{sn} for these profiles using an m to n ratio of 0.45, for comparison. Our results deviate from the general trends in this compilation and show the high nonlinearity between k_{sn} and erosion rate, implied by an n of ~7 (Figure 7). Importantly, this analysis nicely illustrates the channel steepness threshold predicted by the stream power parameters recovered from Corinth; these parameters show that fluvial topography in Corinth Rift Eastern Sector is largely insensitive to uplift or erosion rates ≥0.05 mm yr^{-1} (Figure 7).

5.2.3.2. Exploring Hypotheses for high m and n Values

The high m and n values recovered here have important implications not only for the long-term evolution of river profiles in Corinth but also, and more generally, for interpretations of fluvial topography drawn from river profile analysis elsewhere. To further illustrate this point, we begin by conducting a detailed analysis of portions of the four trunk channels that span the knickzone (Figure 8a). We first smooth channel elevations for these portions of the river profile using a 500 m moving window average and calculate the normalized

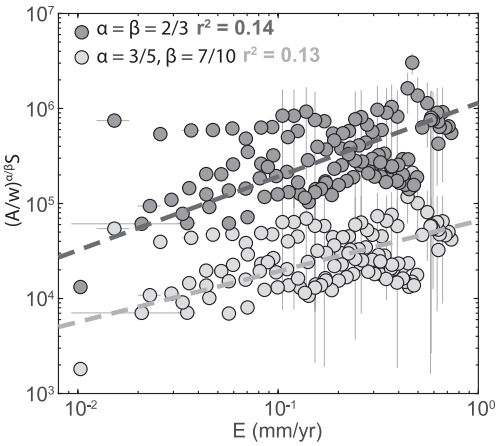

Figure 9. The width-dependent stream power incision model parameter $\left(\frac{A}{w}\right)^{\frac{\alpha}{\beta}} S$ plotted as a function of the best-fit model incision rate. The width-dependent stream power incision model parameter was calculated assuming Manning (light gray) and Darcy-Weisbach (dark gray) frctional relationships. Power-law regression of this data provides constraints on the width-dependent erodibility constant K_w and slope exponent n_w. See text for details.

steepness index, k_{sn}, in 500 m increments. We use two different reference concavities, θ_{ref}, the commonly used value of 0.45 for reference with other studies, and the best-fit concavity from the inversion, approximated to 0.30. Finally, we plot these results against the best-fit model channel incision rates (Figures 8b and 8c).

Results show a poor correlation between k_{sn} and channel incision rate. This poor correlation is not surprising. First, given that the results from the inversion suggest channel steepness is largely insensitive to increases in incision rate beyond ~0.05 mm yr^{-1} (Figures 7, 8b, and 8c). Second, the local k_{sn} data are noisy because k_{sn} is calculated by taking the derivative of χ-elevation data, which amplifies noise in the elevation data. Based on these intriguing results, we seek a deeper understanding of the processes responsible for this apparent decoupling between channel steepness and erosion rate.

Channel Width

We test whether channel width adjustments, which can occur during transient landscape evolution and are not explicitly accounted for in the stream power formulation used here, are responsible for the unusually highly nonlinear scaling between channel steepness and erosion rate. Channel narrowing, along with steepening, acts to locally elevate basal shear stress imparted by a flow, and thus increases the local incision rate. Numerous studies show that channels in many tectonically active settings alter their hydraulic geometry, that is, slope and width, in response to spatial and/or temporal changes in rock uplift rate (Amos & Burbank, 2007; Bender et al., 2019; Cook et al., 2013; Duvall et al., 2004; Finnegan et al., 2005; Whittaker et al., 2007).

Particularly, for river channels thought to be graded and in equilibrium with the rock uplift field, channel width, w, has been shown to scale as a power function of drainage area, A (e.g., Lague, 2014, Montgomery & Gran, 2001):

$$w = k_w A^b \tag{12}$$

where k_w is the width index scaling constant and b is the width exponent. Typical empirically derived values with b range between 0.25 and 0.6 (Lague 2014; Montgomery & Gran, 2001; Yanites & Tucker, 2010). To account for these drainage area-dependent changes in width, the normalized width index, k_{wn}, has been proposed (e.g., Allen et al., 2013; Lague 2014; Yanites & Tucker, 2010):

$$k_{wn} = wA^{-b_{ref}} \tag{13}$$

where b_{ref} is the reference wideness exponent, which is analogous to the reference concavity used in the calculation of the normalized steepness index. However, unlike the reference concavity, there is no widely agreed upon or commonly used value for the reference wideness exponent. Here we follow Lague (2014) and use a value of 0.5 because it makes k_{wn} adimensional.

We use Google Earth™ Imagery and the ChanGeom Matlab scripts (Fisher et al., 2012, 2013) to map approximate channel width along portions of the four trunk channels studied, from the chosen outlet position, through the knickzone, and onto the relict topography above the knickzone (Figure 8a). We emphasize that channel width measurements presented here should be considered as a first-order approximation, given that it was difficult to accurately define them in many locations due to vegetative cover along channel banks. We then calculate and plot k_{wn} against modeled incision rates calculated in 500 m increments along the trunk channel reaches where we mapped channel width (Figure 8d).

Results from this analysis show a moderate negative power law correlation between k_{wn} and incision rate (Figure 8). This relationship indicates that the channels in the Eastern Sector are indeed narrowing to ac-

commodate more rapid rock uplift rates. The k_{wn} versus incision rate data define a power law relationship with an exponent of ~-0.5 for Corinth, which is similar to that shown for various data sets compiled by Lague (2014); however, the values of k_{wn} here are about an order of magnitude lower than those reported by Lague (2014) for comparable incision rates.

To take this analysis a step further, we use our width measurements and best-fit incision model from the inversion to empirically calibrate a version of the stream power model with explicit inclusion of channel width (e.g., Deal et al., 2018; Lague, 2014). A simplified version of the width-dependent stream power model can be described by:

$$E = K_w \left(\left(\frac{A}{w} \right)^{\frac{\alpha}{\beta}} S \right)^{n_w} \tag{14}$$

The subscript w on K and n identify these as width-based equivalents of the erodibility and slope exponent in Equation 3. The two new parameters, α and β, depend on the frictional relationship used. Assuming a Manning relationship, $\alpha = 3/5$ and $\beta = 7/10$ and, assuming a Darcy-Weisbach relation, $\alpha = \beta = 2/3$. These values suggest that the exponent on the width-normalized drainage area term is between ~0.86 and 1. To determine K_w and n_w, we first calculate the $\left(\frac{A}{w} \right)^{\frac{\alpha}{\beta}} S$ assuming two different $\frac{\alpha}{\beta}$ values of 0.86 and 1 and then conduct a power law regression through these values and the modeled incision rates (Figure 9). Results show that K_w is 9.31×10^{-13} and 1.53×10^{-11} and n_w is 1.87 and 1.29 for each $\frac{\alpha}{\beta}$ value, respectively. The fits are not particularly strong, with r-squared values of 0.13 and 0.14, respectively.

The relatively poor fit between the width-dependent incision parameter and modeled incision rate suggests that channel narrowing partially explains the inverse modeling results. Nonetheless, several relevant conclusions can be drawn from the channel width analysis. First, this analysis shows the width-dependent slope exponent n_w is within the typically observed range, suggesting that the effects of channel narrowing mostly account for the high slope and drainage area exponents in the generic stream power model of Equation 3. Second, it indicates that, at least for the Eastern Sector of Corinth, channel narrowing appears a dominant mechanism by which channels adjust their hydraulic geometry to accommodate transient adjustment to tectonic forcing. This finding is consistent with the detailed analysis of channel hydraulic geometry conducted by Zondervan et al. (2020) in the Vouraikos catchment several tens of kilometers to the west of the rivers studied here. However, we note that channel width adjustments are dynamic and can sweep upstream with a migrating knickpoint (e.g. Lague, 2014). It is likely that dynamic width adjustments are at play in the Corinth rivers, which complicates our width analysis, which only represents a snapshot in time. We return to this point in the following section of the discussion.

Other Potential Mechanisms

Many other mechanisms are not explicitly accounted for by our models, and that might impact our results and help explain the high n and m values recovered by the inverse model. For example, sediment flux and transport are important in bedrock erosion (Attal et al., 2015; Cook et al., 2013; Finnegan et al., 2007; Shobe et al., 2016; Sklar & Dietrich, 2004; Whittaker et al., 2007). Sediment can act to enhance erosion rate by providing tools to abrade bedrock, or it can work to inhibit incision by armoring the river bed (e.g., Sklar & Dietrich, 1998, 2004). Provided full coupling between river channels and adjacent hillslopes, and assuming local sediment supply to the channels is proportional to the river incision rate, increased sediment supply might locally elevate erosional efficiency through the delivery of abrading tools. In this case, one would expect a nonlinear relationship between k_{sn} and erosion rate, that is, as the erosion rate increases, k_{sn} becomes progressive less sensitive to changes in erosion rate.

The incision model used here also ignores the potential role of incision thresholds, which predict nonlinearity ($n > 1$) in channel steepness and incision rate relationships (Deal et al., 2018; DiBiase & Whipple, 2011; Lague et al., 2005; Scherler et al., 2017; Snyder et al., 2003; Tucker, 2004; Tucker & Bras, 2000). Such nonlinearity generally arises because as channel steepness increases, so does the range of floods capa-

ble of mobilizing channel-armoring bedload. We expect incision thresholds to be relatively low in the Eastern Sector, given that the highly erodible and friable nature of the generally fine-grained bedrock is likely to generate small bedload grain sizes. This assertion is supported by grain size measurements from Watkins et al. (2020), who report median grain size (D_{50}) measurements for rivers in the Eastern Sector ranging from ~1 to 20 mm, implying low incision thresholds. Nonetheless, it is likely that incision thresholds and the distribution of threshold breeching floods play a role in explaining our findings.

An important aspect of interpreting the results comes from the pattern of river network elevation residuals; the best-fit model fits the data well in the lower reaches within the knickzone but poorly reproduces channel elevations at low drainage areas above the knickzone (Figures 4a and 4b). Some of this mismatch might be attributed to factors such as drainage divide migration that are ignored in our modeling. However, it is also possible that these low-drainage-area misfits are the result of m and n varying along the river channels. In our case, the recovered m and n parameters are weighted to the knickzone because most data lie within this transient portion of the river network. The best-fit m and n values, therefore, might not be representative of portions of the channel network adjusted to the pre-rifting uplift field preserved above the knickzone.

Using a stream power incision model that accounts for dynamic changes in channel width, bank erosion, a stochastic distribution of floods, and incision thresholds, Lague (2014) showed that the slope exponent n varies along a modeled river profile during transient landscape evolution (see Figure 7 of Lague, 2014). In these simulations, channels narrow and steepen within the knickpoint as it migrates upstream. Channel narrowing and steepening results in a drop in the incision threshold and n within the knickpoint. Interestingly, in the downstream wake of the passing knickpoint, the re-equilibration response time of the channel to knickpoint passage results in a concave reach where the slope exponent increases relative to the initial condition. As noted by Lague (2014), aspects of these simulations need to be vetted with field data; however, they suggest that n can reach high values downstream of a transient knickpoint. Within the context of Lague's (2014) numerical models, high n values might simply reflect the downstream re-equilibration phase in transient channels. If correct, n is spatially variable (and by association m) along channels in Corinth, which can help explain the high misfits in channel heads above the knickzones (Figures 4a and 4b).

Another possibility is that the detachment-limited stream power incision model is perhaps not the best long-term landscape evolution model to describe the Eastern Sector rivers. For example, both Tallings (2000) and Cowie et al. (2008) found that in easily eroded bedrock, similar to that of the Corinth basin-fill units, river incision proceeds in a manner better approximated by the transport-limited steam power model end member relative to the detachment-limited end-member assumed here. Such a hypothesis emphasizes the need for more detailed, field-based studies of these rivers.

5.3. Implications and Future Work

The most relevant results from our inversion are the predicted fault initiation timing and the high m and n values in the stream power model. Our research indicates the CFS initiated at ~0.6 Ma in the eastern portion of the rift. This time of fault initiation aligns with a growing body of literature pinning down the onset of the rapid and localized Middle Pleistocene rifting in Corinth (e.g., de Gelder et al., 2019; McNeill et al., 2019; Nixon et al., 2016). Still, further research and new data sets are needed to provide additional constraints in westward portions of the rift margin. Such studies will ultimately lead to better determinations of the onset time and lateral growth history of the Corinth Fault System, which is time transgressive along strike (Fernández-Blanco et al. 2019, 2020).

The high m and n values recovered in our analysis are interesting and have important general implications. First, they suggest the relationships between fluvial topography and tectonics might be masked in certain locations. In this study, we are able to show that channel narrowing plays a key role in channel adjustment to tectonic forcing. While channel narrowing helps partially explain the inverse model results, the weak correlation between the width-dependent stream power model and incision rates predicted by the best-fit inverse model suggests that other processes are at play (Figure 9). Although we have not fully explored the implications of dynamically variable channel width, the high misfits at the channel heads indicate that it is an important piece to understanding the response of these, and perhaps other, rivers to tectonic

perturbations (Figures 4a and 4b). The important role of the pattern and rate of tectonic forcing, sediment and incision thresholds, and dynamic width adjustments must be considered collectively when interpreting these findings. Furthermore, we acknowledge that our findings might indicate the detachment-limited stream power model is perhaps not the best choice for the rivers in the Eastern Sector, and that other incision models, such as the transport-limited end member, might better explain the transient evolution of river networks in this setting.

An important implication of this study is that inversions of fluvial topography using a stream power model that assumes a slope exponent, $n = 1$ (Fox et al., 2014; Gallen, 2018; Goren et al., 2014; Pritchard et al., 2009; Roberts & White, 2010; Rudge et al., 2015), might produce biased and potentially inaccurate results. Goren et al. (2014) echo these findings, showing uplift histories are biased when using a linear scheme to invert synthetic topography generated with $n \neq 1$. While the assumption of $n = 1$ is attractive for the use of efficient linear inverse theory, our study shows that this assumption does not apply to the rivers in Corinth. Our results also emphasize the need to formally incorporate data into the inversion of river profiles; otherwise, important aspects of the evolution of topography will be missed, and the resultant tectonic histories possibly biased. In other words, as outlined in Section 2.6, the stream power parameters (i.e., K, n, and m) that determine how topography responses to tectonic forcing can only be defined by relationships between topography and erosion or rock uplift rate and not from river profile data alone.

Finally, another important aspect of this study is that it demonstrates the utility of data-driven, nonlinear inversions of river profiles. Such approaches are flexible and provide an objective framework to test both tectonic and geomorphic models. We demonstrate how these techniques can inform understanding of tectonic processes by extending the geologic record further back in time than is possible with observations and geochronology alone. Furthermore, by leaving the stream power parameters as free variables in the inversion, inverse modeling can pin-point unnoticed parameter values and trade-offs that expand our understanding of both tectonic and geomorphologic processes.

6. Summary and Conclusions

This paper shows how data-driven Bayesian inversions can be used to address questions in tectonics and geomorphology simultaneously and objectively. Our analysis demonstrates that models based on a data-driven Bayesian inversion of river profiles can converge on solutions in a multidimensional space, even with uninformative priors. Importantly, this technique expands the marine terrace record of the tectonic history of the Corinth Rift further back in time and suggests that the rapid ($\sim$1.6 mm yr^{-1}) flexural uplift of the southern rift margin led by the current master fault was active by $\sim$0.6 Ma. The results from the tectonic model are consistent with independent lines of evidence for the rift and allow confidence in results from the geomorphic model that might be perceived as more contentious. While the inversion predicts sediment flux consistent with independent observations, forward models run with the best-fitting parameters find a channel steepness threshold where fluvial topography is insensitive to increases in rock uplift rate above $\sim$0.05 mm yr^{-1}, as defined by unusually high values for the drainage area exponent, m, and the slope exponent, n, of 2.04 and 6.98, respectively. We show that channel narrowing, which is not explicitly accounted for in our inversion, is an important mechanism by which the studied river channels adjust their hydraulic geometry in response to elevated uplift rates. However, this process only partially explains the high m and n values and high degree of nonlinearity recovered by the inverse model, and additional mechanisms, such as dynamic channel width changes, sediment, and incision thresholds, likely play relevant roles. We conclude that nonlinear, data-driven inversions of fluvial topography are of great use to collectively understand tectonic and geomorphic processes.

Data Availability Statement

The data supporting the conclusions can be obtained from de Gelder et al. (2019) and the figures and tables presented in this manuscript and Supporting Information. Details on the SPOT5 DEM data used for our analysis are presented in Fernández-Blanco et al. (2020). These DEM data are under a restrictive academic license and not open for distribution. The "BayesProfiler" codes developed to conduct the data-driven inversion can be cited and found at https://doi.org/10.5281/zenodo.4081849 (https://github.com/sfgallen/bayes_profiler).

Acknowledgments
The authors thank the Colorado State University (CSU) and University of Colorado Boulder Summit High-Performance Computer (HPC) system for access to the HPC computing nodes used for our Bayesian inversions. CSU, the CSU Warner College of Nature Resources, and the CSU Department of Geosciences are thanked for funds that partially supported this research. The authors similarly acknowledge that the research leading to these results has received funding from the People Programme (Marie Curie Actions) of the European Union's Seventh Framework Programme under the ITN project ALErT (Grant FP7-PEOPLE-2013-ITN number 607996). The authors are indebted to Eric Deal, Sam Brooke, Adam Forte, and Associate Editor Mikael Attal for providing excellent and constructive reviews that helped significantly improve an earlier version of this manuscript. In particular, Dr. Deal is credited with suggesting that the channel width analysis that is now presented in Section 5.2.3.2.1 might be critical in explaining our results, for which the authors are grateful. The authors do not have any real or perceived financial conflicts of interest.

References

Allen, G. H., Barnes, J. B., Pavelsky, T. M., & Kirby, E. (2013). Lithologic and tectonic controls on bedrock channel form at the northwest Himalayan front. *Journal of Geophysical Research: Earth Surface*, *118*(3), 1806–1825. https://doi.org/10.1002/jgrf.20113

Amos, C. B., & Burbank, D. W. (2007). Channel width response to differential uplift. *Journal of Geophysical Research*, *112*(F2), F02010. https://doi.org/10.1029/2006JF000672

Anderson, R. S., Densmore, A.L., & Ellis, M. A. (1999). The generation and degradation of marine terraces. *Basin Research*, *11*(1), 7–19. https://doi.org/10.1046/j.1365-2117.1999.00085.x

Armijo, R., Meyer, B., King, G. C. P., Rigo, A., & Papanastassiou, D. (1996). Quaternary evolution of the Corinth Rift and its implications for the Late Cenozoic evolution of the Aegean. *Geophysical Journal International*, *126*(1), 11–53. https://doi.org/10.1111/j.1365-246X.1996.tb05264.x

Aster, R. C., Borchers, B., Thurber, C. H. (2019). Chapter Eleven – Bayesian methods. In R. C. Aster, B. Borchers, C. H. Thurber (Eds.), *Parameter Estimation and Inverse Problems* (Third Edition)(pp. 279–306). Cambridge, MA: Elsevier. https://doi.org/10.1016/B978-0-12-804651-7.00016-X

Attal, M., Mudd, S. M., Hurst, M. D., Weinman, B., Yoo, K., & Naylor, M. (2015). Impact of change in erosion rate and landscape steepness on hillslope and fluvial sediments grain size in the Feather River basin (Sierra Nevada, California). *Earth Surface Dynamics*, *3*(1), 201–222. https://doi.org/10.5194/esurf-3-201-2015

Avallone, A., Briole, P., Agatza-Balodimou, A. M., Billiris, H., Charade, O., Mitsakaki, C., et al. (2004). Analysis of eleven years of deformation measured by GPS in the Corinth Rift Laboratory area. *Comptes Rendus Geoscience*, *336*(4), 301–311. https://doi.org/10.1016/j.crte.2003.12.007

Barnhart, K. R., Tucker, G. E., Doty, S., Shobe, C. M., Glade, R. C., Rossi, M. W., & Hill, M. C. (2020a). Inverting topography for landscape evolution model process representation: Part 2, calibration and validation. *Journal of Geophysical Research: Earth Surface*, *125*, e2018JF004963. https://doi.org/10.1029/2018JF004963

Barnhart, K. R., Tucker, G. E., Doty, S., Shobe, C. M., Glade, R. C., Rossi, M. W., & Hill, M. C. (2020b). Inverting topography for landscape evolution model process representation: Part 3, Determining parameter ranges for select mature geomorphic transport laws and connecting changes in fluvial erodibility to changes in climate. *Journal of Geophysical Research: Earth Surface*, *127*, e2019JF005287. https://doi.org/10.1029/2019JF005287

Barnhart, K. R., Tucker, G. E., Doty, S., Shobe, C. M., Glade, R. C., Rossi, M. W., & Hill, M. C. (2020c). Inverting topography for landscape evolution model process representation: Part 1, conceptualization and sensitivity analysis. *Journal of Geophysical Research: Earth Surface*, *125*, e2018JF004961. https://doi.org/10.1029/2018JF004961

Bayes, T., & Price, N. (1763). An essay towards solving a problem in the doctrine of chances. *Philosophical Transactions of the Royal Society of London*, *53*, 370–418. https://doi.org/10.1098/rstl.1763.0053

Beaumont, C., Fullsack, P., & Hamilton, J. (1992). Erosional control of active compressional orogen. In K. R. McClay (Ed.), *Thurst tectonics* (pp. 1–18). New York, NY: Chapman and Hall. https://doi.org/10.1007/978-94-011-3066-0_1

Bell, R.E. (2008). *Tectonic evolution of the corinth rift(Doctoral thesis)*. University of Southampton, School of Ocean and Earth Science, 227.

Bell, R. E., Duclaux, G., Nixon, C. W., Gawthorpe, R. L., & McNeill, L. C. (2017). High-angle, not low-angle, normal faults dominate early rift extension in the Corinth Rift, central Greece. *Geology*, *46*(2), 115–118. https://doi.org/10.1130/G39560.1

Bender, A. M., Lease, R. O., Haeussler, P. J., Rittenour, T., Corbett, L. B., Bierman, P. R., & Caffee, M. W. (2019). Pace and Process of Active Folding and Fluvial Incision Across the Kantishna Hills Anticline, Central Alaska. *Geophysical Research Letters*, *46*(6), 3235–3244. https://doi.org/10.1029/2018GL081509

Berlin, M. M., & Anderson, R. S. (2007). Modeling of knickpoint retreat on the Roan Plateau, western Colorado. *Journal of Geophysical Research: Earth Surface*, *112*(F3) https://doi.org/10.1029/2006JF000553

Billiris, H., Paradissis, D., Veis, G., England, P., Featherstone, W., Parsons, B., et al. (1991). Geodetic determination of tectonic deformation in central Greece from 1900 to 1988. *Nature*, *350*(6314), 124–129. https://doi.org/10.1038/350124a0

Bonneau, M. (1984). Correlation of the Hellenide nappes in the south-east Aegean and their tectonic reconstruction. *Geological Society, London, Special Publications*, *17*(1), 517–527. https://doi.org/10.1144/GSL.SP.1984.017.01.38

Brasier, A. T., Aandrews, J. E., & Kendall, A. C. (2011). Diagenesis or dire genesis? The origin of columnar spar in tufa stromatolites of central Greece and the role of chironomid larvae. *Sedimentology*, *58*(5), 1283–1302. https://doi.org/10.1111/j.1365-3091.2010.01208.x

Braun, J., & Willett, S. D. (2013). A very efficient O(n), implicit and parallel method to solve the stream power equation governing fluvial incision and landscape evolution. *Geomorphology*, 180–181, 170–179. https://doi.org/10.1016/j.geomorph.2012.10.008

Causse, C., Moretti, I., Eschard, R., Micarelli, L., Ghaleb, B., & Frank, N. (2004). Kinematics of the Corinth Gulf inferred from calcite dating and syntectonic sedimentary characteristics. *Comptes Rendus Geoscience*, *336*(4), 281–290. https://doi.org/10.1016/j.crte.2003.11.017

Collier, R. E. L. (1990). Eustatic and tectonic controls upon Quaternary coastal sedimentation in the Corinth Basin, Greece. *Journal of the Geological Society*, *147*(2), 301–314. https://doi.org/10.1144/gsjgs.147.2.0301

Collier, R. E. L., Leeder, M. R., Rowe, P. J., & Atkinson, T. C. (1992). Rates of tectonic uplift in the Corinth and Megara Basins, central Greece. *Tectonics*, *11*(6), 1159–1167. https://doi.org/10.1029/92TC01565

Cook, K. L., Turowski, J. M., & Hovius, N. (2013). A demonstration of the importance of bedload transport for fluvial bedrock erosion and knickpoint propagation. *Earth Surface Processes and Landforms*, *38*(7), 683–695. https://doi.org/10.1002/esp.3313

Cowie, P. A., Whittaker, A. C., Attal, M., Roberts, G., Tucker, G. E., & Ganas, A. (2008). New constraints on sediment-flux-dependent river incision: Implications for extracting tectonic signals from river profiles. *Geology*, *36*(7), 535–538. https://doi.org/10.1130/G24681A.1

Croissant, T., & Braun, J. (2014). Constraining the stream power law: A novel approach combining a landscape evolution model and an inversion method. *Earth Surface Dynamic*, *2*(1), 155–166. https://doi.org/10.5194/esurf-2-155-2014

Crosby, B. T., & Whipple, K. X. (2006). Knickpoint initiation and distribution within fluvial networks: 236 waterfalls in the Waipaoa River, North Island, New Zealand. *Geomorphology*, *82*(1), 16–38. https://doi.org/10.1016/j.geomorph.2005.08.023

Cyr, A. J., Granger, D. E., Olivetti, V., & Molin, P. (2010). Quantifying rock uplift rates using channel steepness and cosmogenic nuclide–determined erosion rates: Examples from northern and southern Italy. *Lithosphere*, *2*(3), 188–198. https://doi.org/10.1130/L96.1

de Gelder, G., FernÃ¡ndez-Blanco, D., Melnick, D., Duclaux, G., Bell, R. E., Jara-Muñoz, J., et al. (2019). Lithospheric flexure and rheology determined by climate cycle markers in the Corinth Rift. *Scientific Reports*, *9*(1), 4260. https://doi.org/10.1038/s41598-018-36377-1

Deal, E., Braun, J., & Botter, G. (2018). Understanding the Role of Rainfall and Hydrology in Determining Fluvial Erosion Efficiency. *Journal of Geophysical Research: Earth Surface*, *123*(4), 744–778. https://doi.org/10.1002/2017JF004393

Demoulin, A., Beckers, A., & Hubert-Ferrari, A. (2015). Patterns of Quaternary uplift of the Corinth rift southern border (N Peloponnese, Greece) revealed by fluvial landscape morphometry. *Geomorphology*, *246*, 188–204. https://doi.org/10.1016/j.geomorph.2015.05.032

Dia, A. N., Cohen, A. S., O'Nions, R. K., & Jackson, J. A. (1997). Rates of uplift investigated through 230Th dating in the Gulf of Corinth (Greece). *Chemical Geology*, *138*(3), 171–184. https://doi.org/10.1016/S0009-2541(97)00010-7

DiBiase, R. A., & Whipple, K. X. (2011). The influence of erosion thresholds and runoff variability on the relationships among topography, climate, and erosion rate. *Journal of Geophysical Research*, *116*(F4) https://doi.org/10.1029/2011JF002095

DiBiase, R. A., Whipple, K. X., Heimsath, A. M., & Ouimet, W. B. (2010). Landscape form and millennial erosion rates in the San Gabriel Mountains, CA. *Earth and Planetary Science Letters*, *289*(1), 134–144. https://doi.org/10.1016/j.epsl.2009.10.036

Duvall, A., Kirby, E., & Burbank, D. (2004). Tectonic and lithologic controls on bedrock channel profiles and processes in coastal California. *Journal of Geophysical Research*, *109*(F3), F03002. https://doi.org/10.1029/2003JF000086

Fernandes, V. M., Roberts, G. G., White, N., & Whittaker, A. C. (2019). Continental-Scale Landscape Evolution: A History of North American Topography. *Journal of Geophysical Research: Earth Surface*, *124*(11), 2689–2722. https://doi.org/10.1029/2018JF004979

Fernández-Blanco, D., de Gelder, G., Lacassin, R., & Armijo, R. (2019). A new crustal fault formed the modern Corinth Rift. *Earth-Science Reviews*, *199*, 102919. https://doi.org/10.1016/j.earscirev.2019.102919

Fernández-Blanco, D., de Gelder, G., Lacassin, R., & Armijo, R. (2020). Geometry of Flexural Uplift by Continental Rifting in Corinth, Greece. *Tectonics*, *39*(1), e2019TC005685. https://doi.org/10.1029/2019TC005685

Finnegan, N. J., Roe, G., Montgomery, D. R., & Hallet, B. (2005). Controls on the channel width of rivers: Implications for modeling fluvial incision of bedrock. *Geology*, *33*(3), 229–232. https://doi.org/10.1130/G21171.1

Finnegan, N. J., Sklar, L. S., & Fuller, T. K. (2007). Interplay of sediment supply, river incision, and channel morphology revealed by the transient evolution of an experimental bedrock channel. *Journal of Geophysical Research*, *112*(F3), F03S11. https://doi.org/10.1029/2006JF000569

Fisher, G. B., Amos, C. B., Bookhagen, B., Burbank, D. W., & Godard, V. (2012). Channel widths, landslides, faults, and beyond: The new world order of high-spatial resolution Google Earth imagery in the study of earth surface processes. In S. J. Whitmeyer, J. E. Bailey, D. G. De Paor, & T. Ornduff (Eds.), *Google Earth and virtual visualizations in geoscience education and research* (Vol. 492, pp. 1–22). Geological Society of America https://doi.org/10.1130/2012.2492(01

Fisher, G. B., Bookhagen, B., & Amos, C. B. (2013). Channel planform geometry and slopes from freely available high-spatial resolution imagery and DEM fusion: Implications for channel width scalings, erosion proxies, and fluvial signatures in tectonically active landscapes. *Geomorphology*, *194*, 46–56. https://doi.org/10.1016/j.geomorph.2013.04.011

Flint, J. J. (1974). Stream gradient as a function of order, magnitude, and discharge. *Water Resources Research*, *10*(5), 969–973. https://doi.org/10.1029/WR010i005p00969

Ford, M., Hemelsdaël, R., Mancini, M., & Palyvos, N. (2017). Rift migration and lateral propagation: Evolution of normal faults and sediment-routing systems of the western Corinth rift (Greece). *Geological Society, London, Special Publications*, *439*(1), 131–168. https://doi.org/10.1144/SP439.15

Ford, M., Rohais, S., Williams, E. A., Bourlange, S., Jousselin, D., Backert, N., & Malartre, F. (2013). Tectono-sedimentary evolution of the western Corinth rift (Central Greece). *Basin Research*, *25*(1), 3–25. https://doi.org/10.1111/j.1365-2117.2012.00550.x

Ford, M., Williams, E. A., Malartre, F., Popescu, S.-M., & Nichols, G. (2007). Stratigraphic architecture, sedimentology and structure of the Vouraikos Gilbert-type fan delta, Gulf of Corinth, Greece. *Sedimentary Processes, Environments and Basins: A Tribute to Peter Friend*, *38*, 49–90. https://doi.org/10.1002/9781444304411.ch4

Fox, M., Goren, L., May, D. A., & Willett, S. D. (2014). Inversion of fluvial channels for paleorock uplift rates in Taiwan. *Journal of Geophysical Research: Earth Surface*, *119*(9), 1853–1875. https://doi.org/10.1002/2014JF003196

Gallen, S. F. (2018). Lithologic controls on landscape dynamics and aquatic species evolution in post-orogenic mountains. *Earth and Planetary Science Letters*, *493*, 150–160. https://doi.org/10.1016/j.epsl.2018.04.029

Gallen, S. F., & Wegmann, K. W. (2017). River profile response to normal fault growth and linkage: An example from the Hellenic forearc of south-central Crete, Greece. *Earth Surface Dynamics*, *5*(1), 161–186. https://doi.org/10.5194/esurf-5-161-2017

Gallen, S. F., Wegmann, K. W., Bohnenstiehl, D. R., Pazzaglia, F. J., Brandon, M. T., & Fassoulas, C. (2014). Active simultaneous uplift and margin-normal extension in a forearc high, Crete, Greece. *Earth and Planetary Science Letters*, *398*, 11–24. https://doi.org/10.1016/j.epsl.2014.04.038

Gallen, S. F., Wegmann, K. W., & Bohnenstiehl, D. W. R. (2013). Miocene rejuvenation of topographic relief in the southern Appalachians. *GSA Today*, *23*(2), 4–11. https://doi.org/10.1130/GSATG163A.1

Gasparini, N. M., & Brandon, M. T. (2011). A generalized power law approximation for fluvial incision of bedrock channels. *Journal of Geophysical Research: Earth Surface*, *116*(F2), F02020. https://doi.org/10.1029/2009JF001655

Gawthorpe, R. L., Leeder, M. R., Kranis, H., Skourtsos, E., Andrews, J. E., Henstra, G. A., et al. (2017). Tectono-sedimentary evolution of the Plio-Pleistocene Corinth rift, Greece. *Basin Research*, *30*(3), 448–479. https://doi.org/10.1111/bre.12260

Gelman, A., Carlin, J. B., Stern, H. S., Dunson, D. B., Vehtari, A., & Rubin, D. B. (2013). *Bayesian data analysis*. Boca Raton, FL: Chapman & Hall/CRC Press.

Glotzbach, C. (2015). Deriving rock uplift histories from data-driven inversion of river profiles. *Geology*, *43*(6), 467–470. https://doi.org/10.1130/G36702.1

Goren, L., Fox, M., & Willett, S. D. (2014). Tectonics from fluvial topography using formal linear inversion: Theory and applications to the Inyo Mountains, California. *Journal of Geophysical Research: Earth Surface*, *119*(8), 1651–1681. https://doi.org/10.1002/2014JF003079

Hack, J. T. (1957). *Studies of longitudinal stream profiles in Virginia and Maryland*. Professional Paper. https://doi.org/10.3133/pp294B

Harel, M.-A., Mudd, S. M., & Attal, M. (2016). Global analysis of the stream power law parameters based on worldwide 10Be denudation rates. *Geomorphology*, *268*, 184–196. https://doi.org/10.1016/j.geomorph.2016.05.035

Harkins, N., Kirby, E., Heimsath, A., Robinson, R., & Reiser, U. (2007). Transient fluvial incision in the headwaters of the Yellow River, northeastern Tibet, China. *Journal of Geophysical Research*, *112*(F3), F03S04. https://doi.org/10.1029/2006JF000570

Hijmans, R. J., Cameron, S. E., Parra, J. L., Jones, P. G., & Jarvis, A. (2005). Very high resolution interpolated climate surfaces for global land areas. *International Journal of Climatology*, *25*(15), 1965–1978. https://doi.org/10.1002/joc.1276

Hilley, G. E., Porder, S., Aron, F., Baden, C. W., Johnstone, S. A., Liu, F., et al. (2019). Earth's topographic relief potentially limited by an upper bound on channel steepness. *Nature Geoscience*, *12*(10), 828–832. https://doi.org/10.1038/s41561-019-0442-3

Howard, A. D. (1994). A detachment-limited model of drainage basin evolution. *Water Resources Research*, *30*(7), 2261–2285. https://doi.org/10.1029/94WR00757

Howard, A. D., Dietrich, W. E., & Seidl, M. A. (1994). Modeling fluvial erosion on regional to continental scales. *Journal of Geophysical Research*, *99*(B7), 13971–13986. https://doi.org/10.1029/94JB00744

Howard, A. D, & Kerby, G (1983). Channel changes in badlands. *GSA Bulletin*, *94*(6), 739–752. https://doi.org/10.1130/0016-7606(1983)94<739:CCIB>2.0.CO2

Jolivet, L., & Brun, J.-P. (2010). Cenozoic geodynamic evolution of the Aegean. *International Journal of Earth Sciences*, *99*(1), 109–138. https://doi.org/10.1007/s00531-008-0366-4

Jolivet, L., Faccenna, C., Huet, B., Labrousse, L., Le Pourhiet, L., Lacombe, O., et al. (2013). Aegean tectonics: Strain localisation, slab tearing and trench retreat. *Tectonophysics*, 597–598, 1–33. https://doi.org/10.1016/j.tecto.2012.06.011

Karymbalis, E., Papanastassiou, D., Gaki-Papanastassiou, K., Ferentinou, M., & Chalkias, C. (2016). Late Quaternary rates of stream incision in Northeast Peloponnese, Greece. *Frontiers of Earth Science*, *10*(3), 455–478. https://doi.org/10.1007/s11707-016-0577-0

Kirby, E, & Whipple, K (2001). Quantifying differential rock-uplift rates via stream profile analysis. *Geology*, *29*(5), 415–418. https://doi.org/10.1130/0091-7613(2001)029<0415:QDRURV>2.0.CO2

Kirby, E., & Whipple, K. X. (2012). Expression of active tectonics in erosional landscapes. *Journal of Structural Geology*, *44*, 54–75. https://doi.org/10.1016/j.jsg.2012.07.009

Koons, P. O. (1989). The topographic evolution of collisional mountain belts; a numerical look at the Southern Alps, New Zealand. *American Journal of Science* , *289*(9), 1041–1069. https://doi.org/10.2475/ajs.289.9.1041

Lague, D. (2014). The stream power river incision model: evidence, theory and beyond. *Earth Surface Processes and Landforms*, *39*(1), 38–61. https://doi.org/10.1002/esp.3462

Lague, D., Hovius, N., & Davy, P. (2005). Discharge, discharge variability, and the bedrock channel profile. *Journal of Geophysical Research*, *110*(F4), F04006. https://doi.org/10.1029/2004JF000259

Lajoie, K. R. (1986). Coastal tectonics. In R. Wallace (Ed.), *Active tectonics* (pp. 95–124). Washington, DC: National Academy Press.

Le Pichon, X., Angelier, J., Osmaston, M. F., Stegena, L., Vine, F. J., & Smith, A. G. (1981). The Aegean Sea. *Philosophical Transactions of the Royal Society of London. Series A, Mathematical and Physical Sciences*, *300*(1454), 357–372. https://doi.org/10.1098/rsta.1981.0069

Leeder, M. R., McNeill, L. C., Collier, R. E. L., Portman, C., Rowe, P. J., Andrews, J. E., & Gawthorpe, R. L. (2003). Corinth rift margin uplift: New evidence from Late Quaternary marine shorelines. *Geophysical Research Letters*, *30*(12), L14310. https://doi.org/10.1029/2003GL017382

McNeill, L. C., Shillington, D. J., & Carter, G. D. O. & the Expedition 381 Participants. (2019). Corinth Active Rift Development. Proceedings of the International Ocean Discovery Program, *381*. College Station, TX: International Ocean Discovery Program https://doi.org/10.14379/â€‹iodp.proc.381.2019

Merritts, D, & Bull, W. B (1989). Interpreting Quaternary uplift rates at the Mendocino triple junction, northern California, from uplifted marine terraces. *Geology*, *17*(11), 1020–1024. https://doi.org/10.1130/0091-7613(1989)017<1020:IQURAT>2.3.CO;2

Metropolis, N., Rosenbluth, A. W., Rosenbluth, M. N., Teller, A. H., & Teller, E. (1953). Equation of state calculations by fast computing machines. *The Journal of Chemical Physics*, *21*(6), 1087–1092. https://doi.org/10.1063/1.1699114

Miller, S. R., Sak, P. B., Kirby, E., & Bierman, P. R. (2013). Neogene rejuvenation of central Appalachian topography: Evidence for differential rock uplift from stream profiles and erosion rates. *Earth and Planetary Science Letters*, *369*–370, 1–12. https://doi.org/10.1016/j.epsl.2013.04.007

Montgomery, D. R., & Gran, K. B. (2001). Downstream variations in the width of bedrock channels. *Water Resources Research*, *37*(6), 1841–1846. https://doi.org/10.1029/2000WR900393

Morisawa, M. E. (1962). Quantitative geomorphology of some watersheds in the Appalachian Plateau. *GSA Bulletin*, *73*(9), 1025–1046. https://doi.org/10.1130/0016-7606(1962)73[1025:QGOSWI]2.0.CO;2

Nadai, A. (1963). Theory of flow and fracture of solids (Vol. 2). New York, NY: McGraw-Hill.

Nixon, C. W., McNeill, L. C., Bull, J. M., Bell, R. E., Gawthorpe, R. L., Henstock, T. J., et al. (2016). Rapid spatiotemporal variations in rift structure during development of the Corinth Rift, central Greece. *Tectonics*, *35*(5), 1225–1248. https://doi.org/10.1002/2015TC004026

Ori, G. G (1989). Geologic history of the extensional basin of the Gulf of Corinth (?Miocene-Pleistocene), Greece. *Geology*, *17*(10), 918–921. https://doi.org/10.1130/0091-7613(1989)017<0918:GHOTEB>2.3.CO2

Ott, R. F., Gallen, S. F., Wegmann, K. W., Biswas, R. H., Herman, F., & Willett, S. D. (2019). Pleistocene terrace formation, Quaternary rock uplift rates and geodynamics of the Hellenic Subduction Zone revealed from dating of paleoshorelines on Crete, Greece. *Earth and Planetary Science Letters*, *525*, 115757. https://doi.org/10.1016/j.epsl.2019.115757

Ouimet, W. B., Whipple, K. X., & Granger, D. E. (2009). Beyond threshold hillslopes: Channel adjustment to base-level fall in tectonically active mountain ranges. *Geology*, *37*(7), 579–582. https://doi.org/10.1130/G30013A.1

Pechlivanidou, S., Cowie, P. A., Duclaux, G., Nixon, C. W., Gawthorpe, R. L., & Salles, T. (2019). Tipping the balance: Shifts in sediment production in an active rift setting. *Geology*, *47*(3), 259–262. https://doi.org/10.1130/G45589.1

Perron, J. T., & Royden, L. (2013). An integral approach to bedrock river profile analysis. *Earth Surface Processes and Landforms*, *38*(6), 570–576. https://doi.org/10.1002/esp.3302

Pritchard, D., Roberts, G. G., White, N. J., & Richardson, C. N. (2009). Uplift histories from river profiles. *Geophysical Research Letters*, *36*(24), L24301. https://doi.org/10.1029/2009GL040928

Roberts, G. G., & White, N. (2010). Estimating uplift rate histories from river profiles using African examples. *Journal of Geophysical Research: Solid Earth*, *115*(B2), B02406. https://doi.org/10.1029/2009JB006692

Rohais, S., Joannin, S., Colin, J.-P., Suc, J.-P., Guillocheau, F., & Eschard, R. (2007). Age and environmental evolution of the syn-rift fill of the southern coast of the gulf of Corinth (Akrata-Derveni region, Greece). *Bulletin de La Société Géologique de France*, *178*(3), 231–243. https://doi.org/10.2113/gssgfbull.178.3.231

Rudge, J. F., Roberts, G. G., White, N. J., & Richardson, C. N. (2015). Uplift histories of Africa and Australia from linear inverse modeling of drainage inventories. *Journal of Geophysical Research: Earth Surface*, *120*(5), 894–914. https://doi.org/10.1002/2014JF003297

Safran, E. B., Bierman, P. R., Aalto, R., Dunne, T., Whipple, K. X., & Caffee, M. (2005). Erosion rates driven by channel network incision in the Bolivian Andes. *Earth Surface Processes and Landforms*, *30*(8), 1007–1024. https://doi.org/10.1002/esp.1259

Scherler, D., DiBiase, R. A., Fisher, G. B., & Avouac, J.-P. (2017). Testing monsoonal controls on bedrock river incision in the Himalaya and Eastern Tibet with a stochastic-threshold stream power model. *Journal of Geophysical Research: Earth Surface*, *122*(7), 1389–1429. https://doi.org/10.1002/2016JF004011

Schwanghart, W., & Scherler, D. (2014). Short Communication: TopoToolbox 2 – MATLAB-based software for topographic analysis and modeling in Earth surface sciences. *Earth Surf. Dynam.*, *2*(1), 1–7. https://doi.org/10.5194/esurf-2-1-2014

Seger, M., & Alexander, J. (1994). Distribution of Plio-Pleistocene and Modern Coarse-Grained Deltas South of the Gulf of Corinth, Greece. *Tectonic Controls and Signatures in Sedimentary Successions*, *20*, 37–48. https://doi.org/10.1002/9781444304053.ch3

Shobe, C. M., Tucker, G. E., & Anderson, R. S. (2016). Hillslope-derived blocks retard river incision. *Geophysical Research Letters*, *43*(10), 5070–5078. https://doi.org/10.1002/2016GL069262

Sklar, L. S., & Dietrich, W. E. (2004). A mechanistic model for river incision into bedrock by saltating bed load. *Water Resources Research*, *40*(6) https://doi.org/10.1029/2003WR002496

Sklar, L. S., & Dietrich, W. E. (1998). River longitudinal profiles and bedrock incision models: Stream power and the influence of sediment supply. In *Rivers over rock: Fluvial processes in bedrock channels*. AGU. https://doi.org/:10.1029/GM107p0237

Snyder, N. P., Whipple, K. X., Tucker, G. E., & Merritts, D. J. (2002). Interactions between onshore bedrock-channel incision and nearshore wave-base erosion forced by eustasy and tectonics. *Basin Research*, *14*(2), 105–127. https://doi.org/10.1046/j.1365-2117.2002.00169.x

Snyder, N. P., Whipple, K. X., Tucker, G. E., & Merritts, D. J. (2000). Landscape response to tectonic forcing: Digital elevation model analysis of stream profiles in the Mendocino triple junction region, northern California. *GSA Bulletin*, *112*(8), 1250–1263. https://doi.org/10.1130/0016-7606(2000)112<1250:LRTTFD>2.0.CO;2

Snyder, N. P., Whipple, K. X., Tucker, G. E., & Merritts, D. J. (2003). Importance of a stochastic distribution of floods and erosion thresholds in the bedrock river incision problem. *Journal of Geophysical Research*, *108*(B2), 2309. https://doi.org/10.1029/2001JB001655

Sorel, D (2000). A Pleistocene and still-active detachment fault and the origin of the Corinth-Patras rift, Greece. *Geology*, *28*(1), 83–86. https://doi.org/10.1130/0091-7613(2000)28<83:APASDF>2.0.CO2

Stock, J. D., & Montgomery, D. R. (1999). Geologic constraints on bedrock river incision using the stream power law. *Journal of Geophysical Research*, *104*(B3), 4983–4993. https://doi.org/10.1029/98JB02139

Talling, P. J. (2000). Self-organization of river networks to threshold states. *Water Resources Research*, *36*(4), 1119–1128. https://doi.org/10.1029/1999WR900339

Tucker, G. E. (2004). Drainage basin sensitivity to tectonic and climatic forcing: Implications of a stochastic model for the role of entrainment and erosion thresholds. *Earth Surface Processes and Landforms*, *29*(2), 185–205. https://doi.org/10.1002/esp.1020

Tucker, G. E., & Bras, R. L. (2000). A stochastic approach to modeling the role of rainfall variability in drainage basin evolution. *Water Resources Research*, *36*(7), 1953–1964. https://doi.org/10.1029/2000WR900065

Tucker, G. E., & Slingerland, R. (1996). Predicting sediment flux from fold and thrust belts. *Basin Research*, *8*(3), 329–349. https://doi.org/10.1046/j.1365-2117.1996.00238.x

Turner, J. A., Leeder, M. R., Andrews, J. E., Rowe, P. J., Van Calsteren, P., & Thomas, L. (2010). Testing rival tectonic uplift models for the Lechaion Gulf in the Gulf of Corinth rift. *Journal of the Geological Society*, *167*(6), 1237–1250.. https://doi.org/10.1144/0016-76492010-035

Tzedakis, P. C. (1999). The last climatic cycle at Kopais, central Greece. *Journal of the Geological Society*, *156*(2), 425–434. https://doi.org/10.1144/gsjgs.156.2.0425

Tzedakis, P. C., Lawson, I. T., Frogley, M. R., Hewitt, G. M., & Preece, R. C. (2002). Buffered tree population changes in a quaternary refugium: Evolutionary implications. *Science*, *297*(5589), 2044–2047. https://doi.org/10.1126/science.1073083

Watkins, S. E., Whittaker, A. C., Bell, R. E., Brooke, S. A. S., Ganti, V., Gawthorpe, R. L., et al. (2020). Straight from the source's mouth: Controls on field-constrained sediment export across the entire active Corinth rift, central Greece. *Basin Research*, *32*, 1600–1625. https://doi.org/10.1111/bre.12444

Watkins, S. E., Whittaker, A. C., Bell, R. E., McNeill, L. C., Gawthorpe, R. L., Brooke, S. A. S., & Nixon, C. W. (2018). Are landscapes buffered to high-frequency climate change? A comparison of sediment fluxes and depositional volumes in the Corinth Rift, central Greece, over the past 130 k.y. *GSA Bulletin*, *131*(3–4), 372–388. https://doi.org/10.1130/B31953.1

Watts, A. B. (2001). *Isostasy and flexure of the lithosphere*. Cambridge: Cambridge University Press.

Whipple, K. X. (2004). Bedrock rivers and the geomorphology of active orogens. *Annual Review of Earth and Planetary Sciences*, *32*(1), 151–185. https://doi.org/10.1146/annurev.earth.32.101802.120356

Whipple, K. X., Forte, A. M., DiBiase, R. A., Gasparini, N. M., & Ouimet, W. B. (2017). Timescales of landscape response to divide migration and drainage capture: Implications for the role of divide mobility in landscape evolution. *Journal of Geophysical Research: Earth Surface*, *122*(1), 248–273. https://doi.org/10.1002/2016JF003973

Whipple, K. X, Hancock, G. S, & Anderson, R. S (2000). River incision into bedrock: Mechanics and relative efficacy of plucking, abrasion, and cavitation. *GSA Bulletin*, *112*(3), 490–503. https://doi.org/10.1130/0016-7606(2000)112<490:RIIBMA>2.0.CO2

Whipple, K. X., & Tucker, G. E. (1999). Dynamics of the stream-power river incision model: Implications for height limits of mountain ranges, landscape response timescales, and research needs. *Journal of Geophysical Research*, *104*(B8), 17661–17674. https://doi.org/10.1029/1999JB900120

Whittaker, A. C., Cowie, P. A., Attal, M., Tucker, G. E., & Roberts, G. P. (2007). Bedrock channel adjustment to tectonic forcing: Implications for predicting river incision rates. *Geology*, *35*(2), 103–106. https://doi.org/10.1130/G23106A.1

Wobus, C., Whipple, K. X., Kirby, E., Snyder, N., Johnson, J., Spyropolou, K., et al. (2006). Tectonics from topography: Procedures, promise, and pitfalls. In S. D. Willett, N. Hovius, M. T. Brandon, & D. M. Fisher (Eds.), *Tectonics, climate, and landscape evolution* (Vol. 398, pp. 0). Geological Society of America. https://doi.org/10.1130/2006.2398(04

Yanites, B. J., & Tucker, G. E. (2010). Controls and limits on bedrock channel geometry. *Journal of Geophysical Research: Earth Surface*, *115*(F4), F04019. https://doi.org/10.1029/2009JF001601

Zelilidis, A. (2000). Drainage evolution in a rifted basin, Corinth graben, Greece. *Geomorphology*, *35*(1), 69–85. https://doi.org/10.1016/S0169-555X(00)00023-4

Zondervan, J. R., Whittaker, A. C., Bell, R. E., Watkins, S. E., Brooke, S. A. S., & Hann, M. G. (2020). New constraints on bedrock erodibility and landscape response times upstream of an active fault. *Geomorphology*, *351*, 106937. https://doi.org/10.1016/j.geomorph.2019.106937